

Supporting Information

Graphitic Dots Combining Photophysical Characteristics of Organic Molecular Fluorophores and Inorganic Quantum Dots

Raphaël de Boëver^{a,b}, Adam Langlois^c, Xu Li^{b*} & Jerome P. Claverie^{a*}

^aDepartment of Chemistry, Université de Sherbrooke, Sherbrooke, Québec J1K 2R1, Canada

^bInstitute of Materials Research & Engineering (A*STAR), 2 Fusionopolis Way, Innovis, #08-03, Singapore 138634

^cDepartment of Chemistry and Biochemistry, University of Windsor, Windsor, Ontario N9B 3P4, Canada

*Corresponding authors: x-li@imre.a-star.edu.sg; jerome.claverie@usherbrooke.ca

Table of content

Experimental Section	4-9
Fig. S1 ^1H NMR spectrum of P(TBA).	10
Fig. S2 ^1H NMR spectrum of P(TBA- <i>b</i> -PFPA).	10
Fig. S3 ^{19}F NMR spectra of PFPA monomer and P(TBA- <i>b</i> -PFPA).	11
Fig. S4 ^1H NMR spectrum of P(TBA- <i>b</i> -AGA).	11
Fig. S5 ^{19}F NMR spectrum of P(TBA- <i>b</i> -AGA).	12
Fig. S6 Size-exclusion chromatograms of P(TBA) and P(TBA- <i>b</i> -PFPA) in THF.	12
Fig. S7 FTIR spectra of P(TBA), P(TBA- <i>b</i> -PFPA), P(TBA- <i>b</i> -AGA) and MFGDs.	13
Table S1 FTIR bands assignment for P(TBA), P(TBA- <i>b</i> -PFPA), P(TBA- <i>b</i> -AGA) and MFGDs.	14
Fig. S8 TEM images of P(TBA- <i>b</i> -AGA) reverse-micelles in a DMSO:1-heptanol (1:2, v:v) mixture.	15
Fig. S9 DLS size distribution of P(TBA- <i>b</i> -AGA) reverse-micelles in various DMSO:1-heptanol mixtures.	15
Fig. S10 TGA curve of P(TBA).	16
Fig. S11 Temperature of the emulsion as a function of time during the graphitization step.	16
Fig. S12 Zeta potential as a function of pH for MFGDs in various aqueous buffers.	17
Fig. S13 TGA curves of raw MFGDs and purified MFGDs.	17
Fig. S14 Photographs of MFGDs in various solvents, with and without exposure to sunlight.	18
Fig. S15 TEM images of dispersed MFGDs.	19
Fig. S16 Size distribution histogram of MFGDs (from TEM images).	19
Fig. S17 HR-TEM images of isolated MFGDs.	20
Fig. S18 Size-exclusion chromatogram of MFGDs in THF.	20
Fig. S19 O1s XPS spectrum of MFGDs.	21
Fig. S20 Survey XPS spectrum of MFGDs.	21
Fig. S21 N1s XPS spectrum of MFGDs.	22
Fig. S22 Mott-Schottky plot for MFGDs dropcasted on FTO.	23
Fig. S23 Photographs of dried MFGDs as a dark brick-red fine powder.	23
Fig. S24 PL spectra and photographs of MFGDs in DMF and in water, at various excitation wavelengths.	24
Fig. S25 3D PL map of MFGDs in solution in DMF, in solution in water and dispersed in a PVDF film.	25
Fig. S26 PL spectra in DMF from graphitization control experiments using different precursors or solvents.	26
Fig. S27 Photographs of MFGDs at different concentrations in DMF, under ambient light or white LED excitation. Emission color and PL spectra of MFGDs in DMF as a function of their concentration.	27
Fig. S28 Emission color and PL spectra of MFGDs in DMF as a function of the excitation wavelength.	28
Fig. S29 Scattered light intensity as a function of wavelength for MFGDs in DMF and for the blank. Corresponding calculated and transmission-measured UV-vis absorption spectra.	28

Fig. S30	UV-vis absorption spectra of MFGDs in DMF at different dilution. Associated Beer-Lambert plots.	29
Fig. S31	Schematic representation of a “standard” and a “front-facing” configurations for PL measurement. Schematic representation of the corresponding and classically encountered filter effects.	30
Fig. S32	PL spectra of concentrated (as-prepared) MFGDs in DMF using a “standard” or a “front-facing” configuration.	30
Fig. S33	Quantum yield measurements from an integrating sphere with a 470 nm excitation.	31
Fig. S34	Quantum yield measurements from an integrating sphere with a 485 nm excitation.	32
Fig. S35	Quantum yield measurements from an integrating sphere with a 500 nm excitation.	34
Fig. S36	TCSPC decay traces, fits, lifetime distributions - MFGDs in DMF ($\lambda_{\text{ex}} = 477 \text{ nm}$, $\lambda_{\text{em}} = 547 \text{ nm}$).	34
Fig. S37	TCSPC decay traces, fits, lifetime distributions - MFGDs in DMF ($\lambda_{\text{ex}} = 477 \text{ nm}$, $\lambda_{\text{em}} = 598 \text{ nm}$).	35
Table S2	PL lifetime fits (distribution analysis) - MFGDs in DMF ($\lambda_{\text{ex}} = 477 \text{ nm}$, $\lambda_{\text{em}} = 547 \text{ nm}$).	36
Table S3	PL lifetime fits (distribution analysis) - MFGDs in DMF ($\lambda_{\text{ex}} = 477 \text{ nm}$, $\lambda_{\text{em}} = 598 \text{ nm}$).	36
Fig. S38	TCSPC decay traces, fits, lifetime distributions - MFGDs in DMF ($\lambda_{\text{ex}} = 397 \text{ nm}$, $\lambda_{\text{em}} = 485/547 \text{ nm}$).	37
Table S4	PL lifetime fit (distribution analysis) - MFGDs in DMF ($\lambda_{\text{ex}} = 397 \text{ nm}$, $\lambda_{\text{em}} = 485/547 \text{ nm}$).	38
Table S5	PL lifetime fit (exponential component analysis) - MFGDs in DMF ($\lambda_{\text{ex}} = 477 \text{ nm}$, $\lambda_{\text{em}} = 485/547 \text{ nm}$).	38
Fig. S39	fs-TAS maps and kinetic traces of MFGDs in DMF ($\lambda_{\text{pump}} = 530 \text{ nm}$).	39
Fig. S40	fs-TAS maps and kinetic traces of MFGDs in DMF ($\lambda_{\text{pump}} = 480 \text{ nm}$).	40
Fig. S41	fs-TAS maps and kinetic traces of MFGDs in DMF ($\lambda_{\text{pump}} = 397 \text{ nm}$).	41
Table S6	fs-TAS deconvolution results of MFGDs in DMF ($\lambda_{\text{pump}} = 530 \text{ nm}$, 480 nm and 397 nm).	42
Fig. S42	fs-TAS kinetic traces on a 7-ps window of MFGDs in DMF ($\lambda_{\text{pump}} = 530 \text{ nm}$, 480 nm , 397 nm).	43
Fig. S43	Decay associated spectra (DAS) from fs-TAS measurements ($\lambda_{\text{pump}} = 530 \text{ nm}$, 480 nm , 397 nm).	44
Fig. S44	Photograph of a vial containing an aqueous acrylamide-gel dispersing MFGDs. Mounted glass-walled pool on a microscope slide designed for MFGDs microscopy studies: before and after curing.	45
Fig. S45	Wide-field fluorescence micrographs of MFGDs dispersed in an aqueous acrylamide gel.	45
Fig. S46	PL spectra of MFGDs in aqueous buffers of different pH at various excitation wavelengths.	46
Fig. S47	Transient polarized fluorescence decays of MFGDs in DMF with residuals and autocorrelation of the residuals acquired from vertically polarized light ($\lambda_{\text{ex}} = 479 \text{ nm}$ and $\lambda_{\text{ex}} = 510 \text{ nm}$)	47
Table S7	Transient polarized fluorescence decay fits – MFGDs in DMF ($\lambda_{\text{ex}} = 479 \text{ nm}$, $\lambda_{\text{ex}} = 510 \text{ nm}$).	48
Fig. S48	Steady-state polarized fluorescence spectra (I_{VV} , I_{VH} , I_{HH} , I_{HV}) and resulting fluorescence anisotropy.	49
References		50

Experimental Section

Chemical and Polymer analysis. Nuclear magnetic resonance (NMR) spectra (^1H , ^{19}F) were acquired using a JEOL ECA II (500 MHz) instrument, whereas Fourier transform Infrared (FTIR) spectra were acquired using a Perkin Elmer Spectrum 2000 FTIR spectrometer. Size-exclusion chromatography (SEC) and molecular weights (M_n , M_w) determination was performed using a Malvern Panalytical Viscotek TDA 305 with a $0.4\text{ mL}\cdot\text{min}^{-1}$ THF flow as the mobile phase (stabilized with BHT), $100\text{ }\mu\text{L}$ as volume injection ($C = 2\text{ mg}\cdot\text{mL}^{-1}$). Thermogravimetric analysis of P(TBA) was performed on a Netzsch STA 449 F1 Jupiter simultaneous thermal analyzer (heat-up rate of $2^\circ\text{C}\cdot\text{min}^{-1}$). The sample room atmosphere was pre-purged using argon prior to any analysis. A continuous argon flow is kept during the measurement to prevent any air oxygen from entering the sample room.

Micelles characterization. Micelles hydrodynamic radii were acquired through dynamic light scattering (DLS) measurements performed on a Malvern Zetasizer nano ZS while TEM was used for the sake of further confirmation (See the MFGDs analysis section for TEM conditions). Sample preparation was similar for both techniques: the ready-to-graphitize emulsion was diluted by a factor $\times 100$ in the corresponding DMSO:1-heptanol mixture and subsequently stirred at room temperature for 24h. The resulting dispersion was used for DLS measurements whereas for TEM 3 droplets were successively deposited on a mono-layer graphene Cu grid (EMS or Ted Pella) and sucked out using a Kimtech wipe. The wet grid was then allowed to dry at room temperature for 24h.

MFGDs analysis. FTIR spectrum of the MFGDs was also acquired using a Perkin Elmer Spectrum 2000 FTIR spectrometer. Transmission electron microscope (TEM) images were obtained using a FEI Titan (S)TEM with an electron acceleration voltage of 200 kV, and a Gatan OneView camera ($4\text{ k} \times 4\text{ k}$ resolution). Images were collected with drift correction and an acquisition time of 1 s at magnifications between $\times 80,000$ and $\times 720,000$. Mono-layer graphene Cu grids (EMS or Ted Pella) were used as MFGDs supports for all the TEM acquisitions. Raman spectrum was acquired using a Witec Alpha 300R confocal Raman microscope. A 532 nm CW pump laser focused by a $\times 100$ microscope objective lens ($\text{NA}=0.65$) was used for excitation and the Raman emission was collected through the same objective. A liquid nitrogen cooled coupled charged device was used for the detection. Solution of CQDs in DMF ($3\text{ mg}\cdot\text{mL}^{-1}$) was drop-casted onto a silicon wafer previously coated with a 5 nm adhesion layer of Ti and a 50 nm layer of Au, both deposited via electron beam evaporation, in order to quench the CQDs photoluminescence in the solid state. Drop-casted substrates are let dry at room temperature for 2 days then heated at 50°C under vacuum for 4 h. X-ray diffraction (XRD) pattern was collected using a Cu $K\alpha$ (8.04 keV) X-ray source on a Bruker D8 Discover instrument. $2\theta = 0.02^\circ$ was chosen as the integration step size. Carbon crystallite length scale was estimated to be around 1.5 nm using Scherrer equation:

$$L = \frac{K\lambda}{\beta \cos \theta} \quad (1)$$

Where L is the mean crystallite size, K a shape factor (assumed to be equal to 0.9), β most-intense peak full-width at half-maximum intensity (corrected from the instrumental broadening), θ Bragg angle of the most intense peak. X-ray photoelectron spectroscopy (XPS) was performed using a Theta Probe (Thermo Scientific) instrument with a monochromatic Al $K\alpha$ (1486.6 eV) X-ray source. Data were fitted using the CasaXPS software (Casa Software, Ltd). MFGDs were filtered on PES or PTFE-membrane syringe filter ($0.2\text{ }\mu\text{m}$), depending on the solvent, prior to any photophysical measurement. Purity assessment of the MFGDs through SEC has been done using the same instrumentation and method as for polymers (injection volume, flow rate...). Thermogravimetric analysis of pure MFGDs was performed using similar instrument as for polymer, with a heat-up rate of $5^\circ\text{C}\cdot\text{min}^{-1}$ instead.

Electrochemical Impedance Spectroscopy (EIS) & Mott-Schottky plot. The electrochemical impedance spectroscopy (EIS) measurement was performed on a Zahner Zennium PP211 photoelectrochemical workstation. The measurement cell consisted of three electrodes immersed in the electrolyte (0.5 M Na₂SO₄ at pH = 7). Namely, the working electrode *i.e.* MFGDs on Fluorine doped Tin Oxide (FTO) glass, the counter electrode *i.e.* a Pt wire and the reference electrode *i.e.* an Ag/AgCl electrode. The working electrode was prepared by dropcasting a solution of MFGDs in ethanol on a FTO square of 9 cm² which was cleaned beforehand with acetone then nanopure water in a sonication bath for 20 min. The working electrode was dried in an oven at 40°C for 16 h then connected to the measurement cell where its surface in contact with the electrolyte was a disc of diameter 1 cm. The potential bias ranged from -1.2 V to 0.8 V (vs NHE) with steps of 40 mV and the frequency ranged from 50 mHz to 4 MHz with a sine wave amplitude of the applied potential of 10 mV. Finally, the Mott-Schottky plot (Figure S21) was reconstructed from the Nyquist plots acquired at every potential bias. From the contact between the working electrode and the electrolyte originates an electrical double layer. The capacitance *C* of such an interface actually covers the contributions from both the MFGDs and the Helmholtz layer in the electrolyte, which can be described respectively by 2 capacitances in series, *C_s* and *C_H*. Assuming that *C_H* ≫ *C_{sc}*, considering the typical layer thickness associated with each capacitance, we have:

$$\frac{A}{C} = A \left(\frac{1}{C_{sc}} + \frac{1}{C_H} \right) \approx \frac{A}{C_{sc}} \quad (2)$$

The n-type semiconductor capacitance is described by the Mott-Schottky equation:

$$\frac{A^2}{C_{sc}^2} = \frac{2}{q\epsilon_0\epsilon_r N_d} \left(E - E_{fb} - \frac{k_B T}{q} \right) \quad (3)$$

Where *q* is the elementary charge, *ε₀* the vacuum permittivity, *ε_r* the relative permittivity of the semiconductor (graphene core), *N_d* the donor density within the semiconductor, *E* the potential bias applied between the working and the reference electrodes, *E_{fb}* the flat band potential of the semiconductor, *k_B* the Boltzmann constant, *T* the absolute temperature. The Mott-Schottky plot (Figure S21) is obtained from equation (2) where *E_{fb}* can be determined as the x-intercept given the linear relationship between 1/*C_{sc}*² and *E* at the negative potential bias. From the resulting slope can be extracted the donor density *N_d*, according to the following derivative:

$$\frac{d\left(\frac{A^2}{C^2}\right)}{dE} = \frac{2}{q\epsilon_0\epsilon_r N_d} \quad (4)$$

A model value of 1000 was chosen for *ε_r* (MFGDs roughly assimilated to graphene oxide) for the sake of estimating the order of magnitude of the donor density *N_d* (Figure S21).

Steady-state spectral measurements. UV-vis absorption spectroscopy was performed on a Shimadzu UV-2501PC spectrophotometer using a 1 cm quartz cuvette. PL spectroscopy was performed using a RF-5301PC spectrofluorophotometer from Shimadzu, a FLS980 phosphorimeter from Edinburgh Instruments or a Fluorolog 3 from Jobin Yvon, all of which using a Xe-lamp as the excitation source. Quantum yield measurements were performed on a Fluorolog 3 from Jobin Yvon equipped with a Quanta-φ integrating sphere. All reported quantum yield measurements were averaged over 4 replicas.

Time-resolved measurements (TRES & TCSPC). Time-resolved emission spectroscopy (TRES) and time-correlated single photon counting at $\lambda_{\text{excitation}} = 477 \text{ nm}$ (TCSPC) measurements were made on a FLS980 phosphorimeter from Edinburgh Instruments using a 477 nm DeltaDiode laser (Horiba scientific) at a repetition rate of 5 MHz as an excitation source with a measured instrument response time of $\sim 175 \text{ ps}$ (= Instrument Response Function FWHM). TCSPC measurements at 395 nm were performed using the SHG of a Ti-Sapphire femtosecond system (Tsunami, Spectra-Physics, 700 mW, 100 fs, 80 MHz, 790 nm) coupled to a custom built pulse picker (Axis Photonique Inc.). Data were acquired with an APD (PDM 50ct, Micro Photon Devices) coupled to a monochromator (CM110, Spectral Products) and a Becker and Hickl PCI counting module (SPC-130).

Femtosecond transient absorption spectroscopy (fs-TAS). Femtosecond transient absorption (fs-TAS) measurements were performed on a homemade system using a Soltice/OPA-800CF (Spectra Physics) Ti-sapphire laser with a 795 nm fundamental output and pulse with of $\sim 75 \text{ fs}$. The pump pulse (excitation) was obtained using the second harmonic of the fundamental output obtained by passing the 795 nm beam through a BBO crystal to obtain a 397 nm excitation or by using an optical parametric amplifier (OPA) which allowed the excitation wavelength to be tuned to 480 nm. All measurements were carried out at a repetition rate of 1 kHz and pulse energies ranging from 78.9 to 360 $\mu\text{J} \cdot \text{cm}^{-2}$ depending on the excitation wavelength and the signal intensity in the probed spectral window. The probe pulse consisted of a white light continuum that was generated by focusing the fundamental laser output onto a sapphire window. An 8 nm delay line was used to introduce a time delay between the pump and probe beams with an accuracy of $\sim 4 \text{ fs}$ and detection was carried out using a custom-made dual CCD camera of 64×1024 pixels sensitive between 200 and 1100 nm (S7030, Spectronic Devices). All the data analysis was performed using the free software Glotaran that allows global analysis of the transient absorption maps. For this work, we used a parallel model permitting the extraction of a sum of independent exponentials that fits the whole 3D transient map: $I(\lambda, t) = C_1(\lambda) e^{-t/\tau_1} + C_2(\lambda) e^{-t/\tau_2} + \dots$.

Steady-state polarization fluorescence spectroscopy. The fluorescence spectra were acquired on a Horiba Quanta Master fluorometer with a xenon lamp and a red enhanced R13456 photomultiplier tube. The dispersions were excited at 480 nm and the fluorescence spectra were acquired from 550 to 700 nm.

Time-resolved polarization fluorescence spectroscopy. The fluorescence decays were acquired with a Horiba DeltaFlex Fluorescence Lifetime Spectrofluorometer. A delta diode laser, with a maximum emission intensity at 479 nm and a repetition rate of 20 MHz, was used to excite the dispersions. The slit width of the emission monochromator was set at 12 nm and the decays were obtained by monitoring the fluorescence intensity at 510 nm. The instrument response function (IRF) was collected at $\lambda_{\text{em}} = \lambda_{\text{ex}} = 479 \text{ nm}$ using an aluminum prism to reflect the excitation beam to the detector.

Zeta potential and PL measurement at various pH. Buffer solutions of different pH were prepared from the following acid/base pairs: citric acid/sodium citrate (pH = 3, 4, 5), disodium hydrogen phosphate /sodium dihydrogen phosphate (pH = 6, 7, 8), sodium bicarbonate/sodium carbonate (pH = 9, 11). Fine adjustment of the pH was done using 0.1M NaOH or 0.1M HCl and controlled through a newly calibrated pH meter. For zeta potential measurement (Figure S12), a few milligrams of MFGDs were stirred in buffers of various pH for 24h prior to analysis. Measurement was performed on a 3P DT-300 instrument. For PL measurements (Figure S46), a concentrated stock solution of MFGDs in DMF is subsequently pipetted in the buffers to obtain aqueous solution of identical MFGDs concentration at various pH. Typically, 100 μL of stock solution is diluted in 10mL of buffer and stored for 24h before analysis. No significant change in pH has been measured after the addition of MFGDs.

MFGDs-containing acrylamide gel preparation for single-nanoparticle microscopy. The MFGDs-containing gel for microscopy study was prepared according to the following procedure. First, a microscopy slide was first mounted with glass gates, forming roughly a 20x15x1 mm³ pool to host the gel precursors. The latter is typically prepared by dissolving acrylamide (400 mg, 5.6 mmol), N,N'-methylenebis(acrylamide) (24 mg, 0.16 mmol), 4,4'-azobis(4-cyanovaleric acid) (0.9 mg, 0.003 mmol) and MFGDs in nanopure water (2 mL). The clear and colorless mixture was bubbled using N₂ for 15 min, poured in the glass pool above the wall level then covered with a glass cover slip. Overflowing solution was sucked-out using a pipet and the whole microscopy slide heated at 70°C in an oven for 2 h.

Single-nanoparticle imaging and temporal fluorescence spectroscopy (microscopy). The immobilized MFGDs were examined through a Plan Apo 60x oil immersion objective NA 1.42 on inverted spectral scanning confocal microscope FV1000 (Olympus, Tokyo, Japan), using a 40 mW Ar-ion laser (488 nm) as the excitation source. Incident laser photons were separated from the MFGDs fluorescence emission using a 405/488 nm dichroic mirror. Fluorescence intensities of lone MFGDs were monitored through the acquisition of 1400 frames at an exposure time of 222 ms/frame. Longer acquisitions of 6000 frames at the same exposure time resulted in identical behaviors *i.e.* neither blinking nor bleaching was observed. This type of measurement was repeated over 20 different and isolated MFGDs, resulting in a similar absence of blinking and photobleaching. Emission data were extracted using FV10-ASW Viewer software whereas presented fluorescence micrographs of MFGDs are intensity-averaged images over time obtained using ImageJ. The “Hi-Lo” lookup table was used to set the maximal signal below saturation, near zero background and optimal dynamic range using the high voltage, offset and gain controls (photomultiplier tube voltage between 600 and 700 V and gain 1x). All data were recorded at room temperature.

Photostability measurement. Photostability measurement was performed on a nanopure water solution of MFGDs (C = 0.1 mg/mL; V = 3.5 mL) pipetted in a 4-window quartz cuvette containing a small stirring bar. The cuvette was placed on a magnetic stirrer sample holder of a Fluorolog 3 from Jobin Yvon, in a 90° configuration to collect the fluoresced photons. The excitation source of the spectrofluorophotometer was a LZ4-00B208 LED from LED Engin (Osram), emitting at 460 nm. The LED was power-supplied from a DC voltage source (12 V) delivering a steady 280 mA current over the whole measurement. The LED emission was collimated through a set of lenses resulting in a measured irradiance of 160 W.m⁻² at the center of the cuvette (irradiated area = 1 cm²). A mini-fan connected to a 24 V DC voltage source kept the LED at a steady temperature. No change in the temperature of the sample room was noticed over the entire measurement. No attempt to degas the MFGDs solution was made.

Materials. All the chemicals involved in the syntheses and media preparation were commercially available and used as received unless otherwise stated. In particular, solvents were used without drying either for the graphitization step (dimethylsulfoxide, 1-heptanol) or for photophysical characterizations (dimethylformamide). Nanopure water ($\rho = 18.2 \text{ M}\Omega\cdot\text{cm}$) was used for synthesis purpose and pH buffer solutions preparation (Figures S12-S42) and as a dispersion media for the MFGDs. Monomers, RAFT agent and 2,2'-azobis (2-methylpropionitrile) thermal free-radical initiator (AIBN) were stored in fridge when not in use. More exactly, TBA monomer was stored as received whereas di-*tert*-butyl-p-cresol (BHT) was added to the freshly synthesized PFFA monomer (0.1 w%) prior to any prolonged storage. Monomers were distilled over additional BHT (1 w%) before polymerization whereas RAFT agent and AIBN were recrystallized respectively from boiling hexane and methanol, then dried under vacuum at room temperature. For the preparation of MFGDs-containing gel 4,4'-azobis (4-cyanovaleric acid) thermal free-radical initiator (ACVA) was recrystallized from boiling methanol.

Synthesis of 2-[[butylsulfanyl]carbonothioyl]sulfanyl} propanoic acid. The RAFT agent was synthesized as reported by Hawke *et al.*¹, with minor modifications. To a biphasic mixture of water (60 mL) and butanethiol (43 mL, 401 mmol) were added NaOH (16 g, 400 mmol, dissolved in 16 mL H₂O) then acetone (20 mL). After full homogenization and cooling down, carbon disulfide (27 mL, 450 mmol) was slowly added with a syringe upon vigorous stirring. The resulting orange solution was stirred for additional 30 min following which the medium was cooled in an ice bath. Using a syringe, 2-bromopropionic acid (37 mL, 410 mmol) was added dropwise and additional NaOH (16.4 g, 410 mmol, dissolved in 16.4 mL H₂O) was subsequently poured slowly. Upon complete cool down, water (60 mL) was added and the whole reaction was stirred overnight at room temperature. Additional water (100 mL) was poured in and the reaction medium was cooled again using an ice bath, following which HCl (~40 mL, ~480 mmol, mixed with 40 mL H₂O) was added at a rate slow enough so that the exotherm did not exceed the room temperature. Upon stirring, still at low temperature, the separating yellow phase solidified and was filtered on Büchner funnel, then thoroughly washed with water while being triturated at the same time. The yellow solid was roughly air-dried on the suction filtration set-up, then vacuum-dried overnight at room temperature. Recrystallization from hexane gave bright yellow fine crystals which were grounded into powder then stored in fridge in a tightly sealed container (82.0 g, η = 86%). ¹H NMR (CDCl₃) δ (ppm): 9.4 (br, CO₂H), 4.87 (q, J = 7.4 Hz, 1H, SCHCH₃), 3.37 (t, J = 7.4 Hz, 2H, CH₂CH₂S), 1.69 (quint, J = 7.4 Hz, 2H, CH₂CH₂S), 1.63 (d, J = 7.4 Hz, 3H, SCHCH₃), 1.44 (sext, J = 7.4 Hz, 2H, CH₃CH₂), 0.94 (t, J = 7.3 Hz, 3H, CH₃CH₂).

Synthesis of PFPA monomer. The PFPA monomer was synthesized according to the procedure reported by Theato *et al.*² with minor modifications. Pentafluorophenol (32.4 g, 176 mmol), then 2,6-lutidine (21 mL, 180 mmol) were dissolved in methylene chloride (200 mL). After cooling the resulting clear solution using an ice bath, acryloyl chloride (14 mL, 172 mmol) was added dropwise. The reaction mixture was stirred for additional 3h in the ice bath, then stirred overnight at room temperature. Precipitated salts were filtered out and the resulting solution was washed with brine (2 \times 70 mL) and dried over MgSO₄. Remaining methylene chloride was removed under vacuum, at room temperature, using a rotary evaporator, and the resulting clear pinkish liquid was subsequently purified through high-vacuum distillation, by gradually increasing the temperature. The first fractions were discarded and the PFPA was finally recovered as a clear colorless liquid (31.4 g, η = 75%). ¹H NMR (CDCl₃) δ (ppm): 6.72 (dd, J = 1.1 and 17.2 Hz, 1H, H_{geminal-trans}), 6.37 (dd, J = 10.5 and 17.2 Hz, 1H, H_{vicinal}), 6.18 (dd, J = 1.1 and 10.5 Hz, 1H, H_{geminal-cis}). ¹⁹F NMR (CDCl₃) (Figure S3) δ (ppm): -152.53 (d, J = 16.8 Hz, 2F, F_{ortho}), -157.92 (t, J = 21.6 Hz, 1F, F_{para}), -162.30 (dd, J = 16.8 and 21.6 Hz, 2F, F_{meta}).

Synthesis of P(TBA) first block. Tert-butyl acrylate (25 mL, 171 mmol), AIBN (41 mg, 0.25 mmol) and RAFT agent (600 mg, 2.5 mmol) were dissolved in 1,4-dioxane (85 mL), and the resulting clear yellow solution was purged for an hour using N₂, under gentle stirring. Polymerization was completed upon heating at 70°C for 2h, still under inert gas protection and slightly more vigorous stirring. The reaction was thermally quenched by pouring the flask in an ethanol/dry-ice bath. Upon warm-up and thaw, the solution was precipitated in cold MeOH:H₂O (8:2, v:v). The recovered bright yellow polymer was purified further through 2 extra dissolution/precipitation cycles, dried under vacuum for 72 h at room temperature, to avoid radicals formation and subsequent crosslinking, then stored in fridge in a tightly sealed container (17.8 g, η = 81%). ¹H NMR (CDCl₃) (Figure S1) δ (ppm): 2.21 (1H, CH₂CH), 1.81 and 1.52 (2H, CH₂CH), 1.43 (9H, H_{tert-butyl}). FTIR (Figure S6A and Table S1). SEC (Figure S7): Mn = 7,500 g.mol⁻¹, PDI = 1.2, Xn (TBA) = 57.

Synthesis of P(TBA-b-PFPA) block copolymer. P(TBA) (3.6 g, 0.48 mmol regarding the RAFT end-group of the chain), AIBN (8 mg, 0.049 mmol) and PFPA (10 g, 42 mmol) were dissolved in 1,4-dioxane (40 mL), and the resulting clear yellow solution was purged for an hour using N₂, under gentle stirring. Polymerization was completed upon heating at 70°C for 8h, still under inert gas protection. The reaction was thermally quenched by pouring the flask in an ethanol/dry-ice bath. Upon warm-up and thaw, the solution was precipitated in cold MeOH:H₂O (9:1, v:v). The recovered white polymer was purified further through 2 extra dissolution/precipitation cycles, dried under vacuum for 72 h at room temperature and stored in fridge in a tightly sealed container (10.7 g, η = 79 %). ¹H NMR (CDCl₃) (Figure S2). ¹⁹F NMR (CDCl₃) (Figure S3) δ (ppm): -153.06 (2F, F_{ortho}), -156.72 (1F, F_{para}), -162.19 (2F, F_{meta}). FTIR (Figure S6B and Table S1). SEC (Figure S8): Mn = 25,000 g.mol⁻¹, PDI = 1.2, Xn (PFPA) = 73.

Synthesis of P(TBA-b-AGA) block copolymer. P(TBA-b-PFPA) (5 g, 14.7 mmol regarding PFPA units) was dissolved in 50 mL DMF. D-(+)-glucosamine hydrochloride (3.49 g, 16.2 mmol) and K₂CO₃ (2.24 g, 16.2 mmol) were grounded and added to the clear orange polymer solution. The grounded solids in suspension were stirred for 2h which resulted in the initial clear orange solution becoming cloudy. Raw solid (polymer + salts) was recovered by precipitation in cold diethyl ether and drying under vacuum at room temperature (9.97 g, η_{raw} = 93%). P(TBA-b-AGA) isolation was done through subsequent purifications: namely, the raw solid was pulverized, suspended in water then centrifuged (twice). The yellow supernatants were discarded whereas the collected straw-colored polymer was finally dried under vacuum at room temperature (4.8 g, η = 96 % as PFPA and AGA have similar molecular weights). **¹H NMR (CDCl₃)** (Figure S4). **¹⁹F NMR (CDCl₃)** (Figure S5, no signal, demonstrating the full substitution of fluorinated esters by N-glucosamines). **FTIR** (Figure S6C and Table S1).

Synthesis of MFGDs. P(TBA-b-AGA) (90 mg) was stirred in DMSO (5 mL) for hours until complete dissolution, after which 1-heptanol (10 mL) was added dropwise under vigorous stirring to give a whitish opalescent emulsion. After further stirring for 24h, the emulsion was transferred to a 50 mL two-neck round-bottom flask topped with a condenser, purged with N₂ for 1h and refluxed at 180°C for 3h, still under inert gas protection. The resulting deep red solution was dried through high vacuum distillation to give the MFGDs as a dark brick-red brittle solid which is easily grounded into fine powder. Purified MFGDs are obtained by first dispersing 60 mg of raw MFGDs in 20 mL of a polar solvent (typically ethanol), then by stirring 24 hours at room temperature, then centrifuging the dispersion at 3000 RPM for 15 min and collecting the clear deep-red supernatant, then filtering the supernatant on a 0.2 μ m PTFE syringe filter and finally drying the solution under vacuum. Purified MFGDs appear as a brick-red powder (Figure S23) (36 mg, purification yield = 60%). **FTIR** (Figure S7D and Table S1).

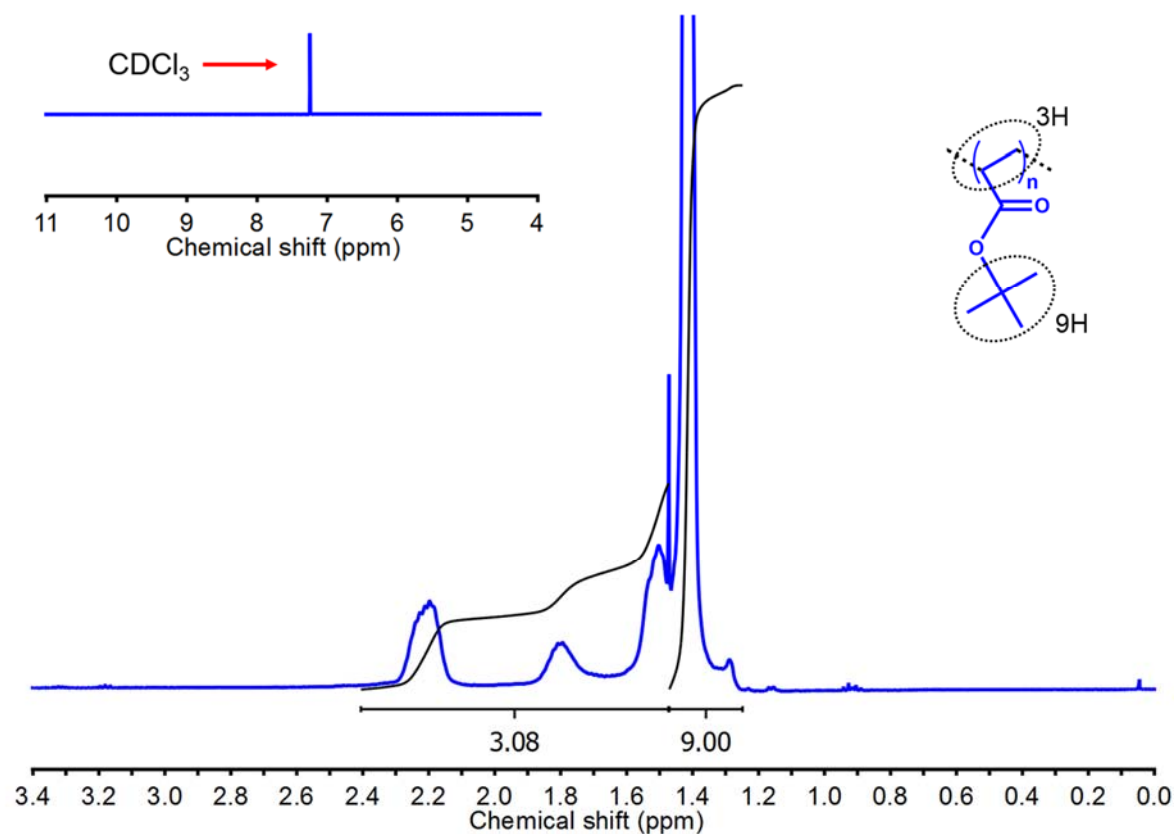


Figure S1. ^1H NMR spectrum of P(TBA) in CDCl_3 .

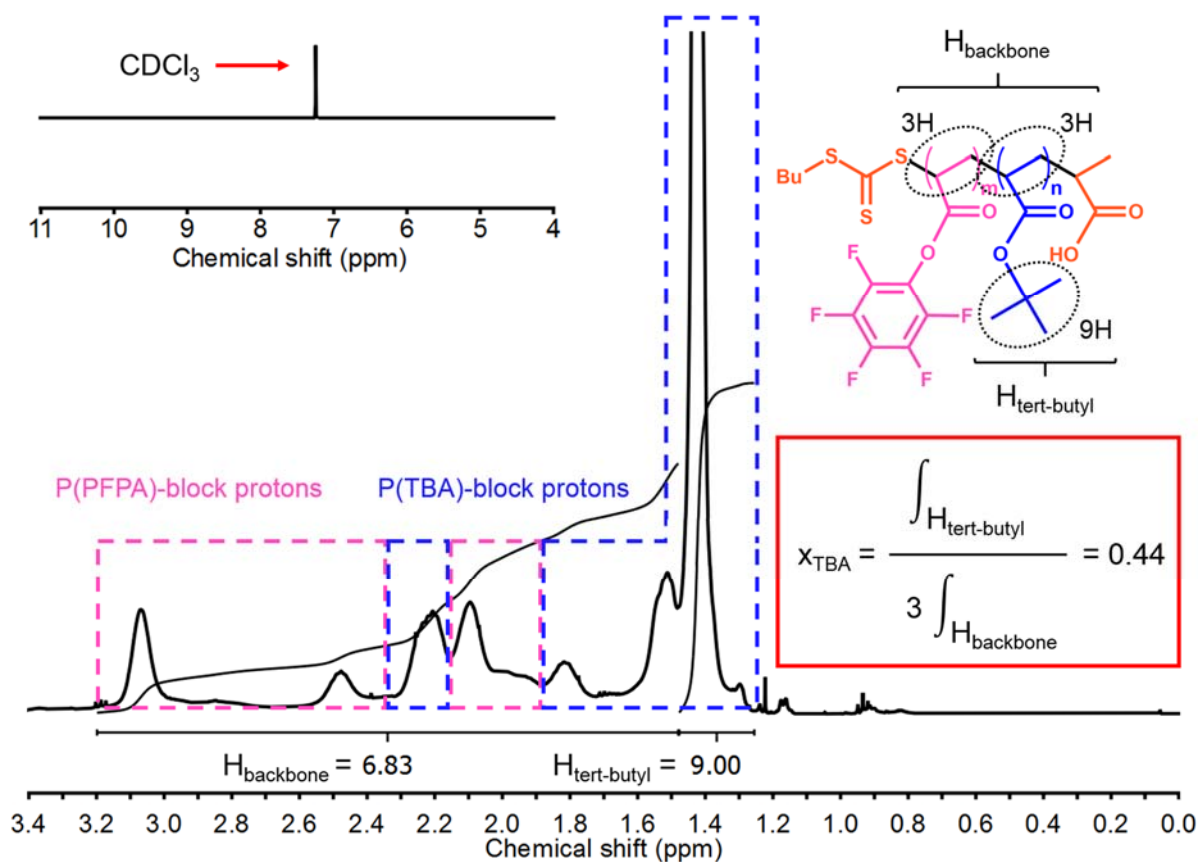


Figure S2. ^1H NMR spectrum of P(TBA-*b*-PFPA) in CDCl_3 .

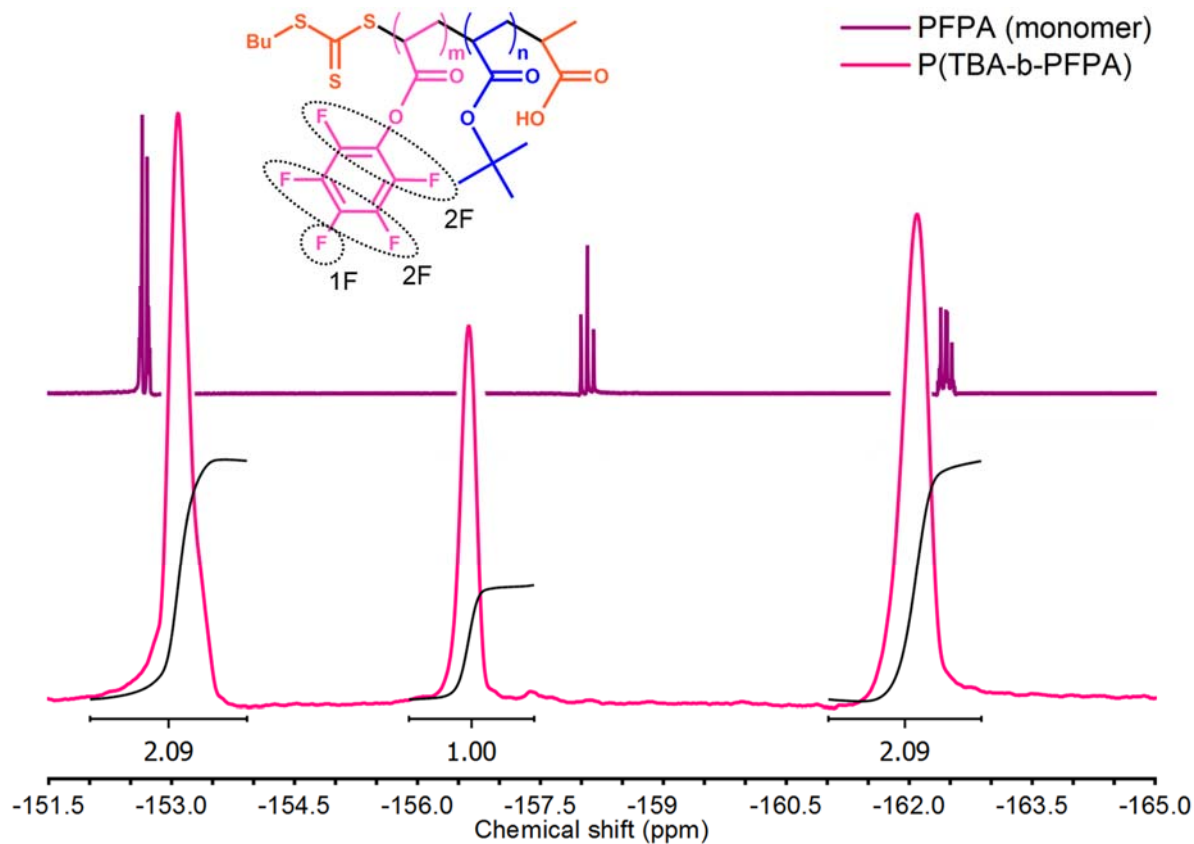


Figure S3. ^{19}F NMR spectra of PFPA monomer (purple) and P(TBA-*b*-PFPA) (pink) in CDCl_3 .

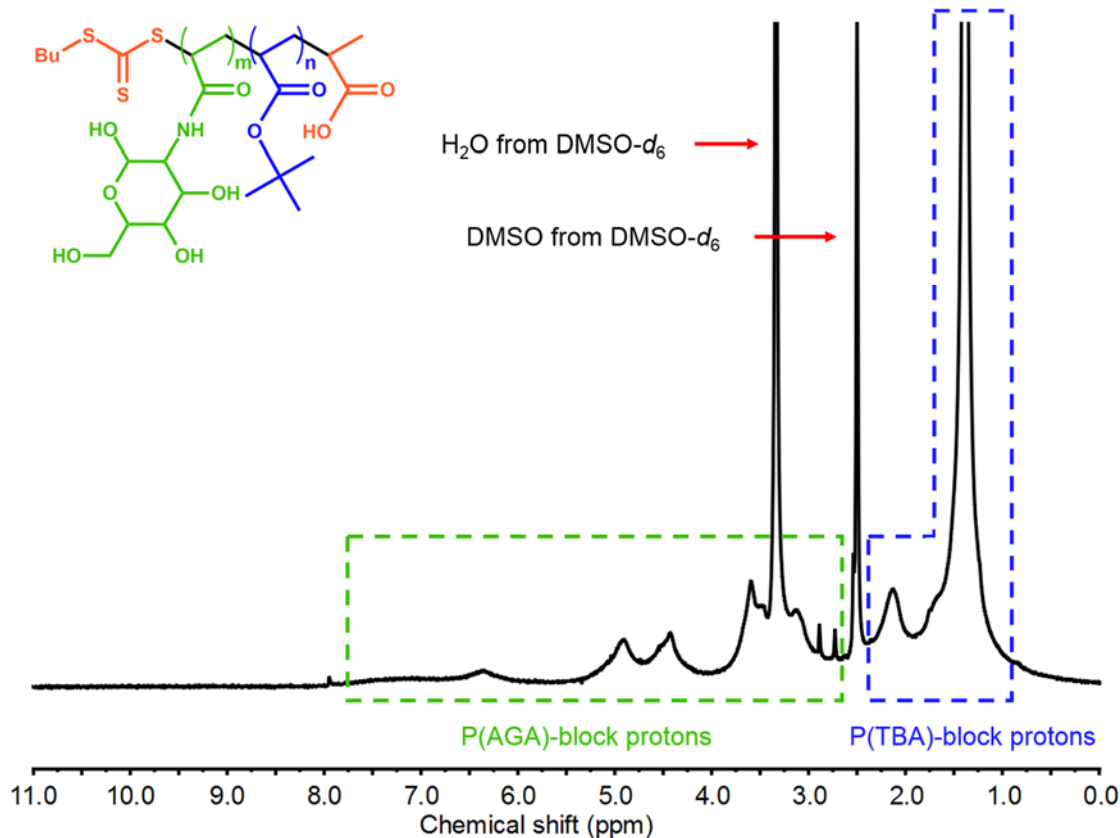


Figure S4. ^1H NMR spectrum of P(TBA-*b*-AGA) in $\text{DMSO}-d_6$.

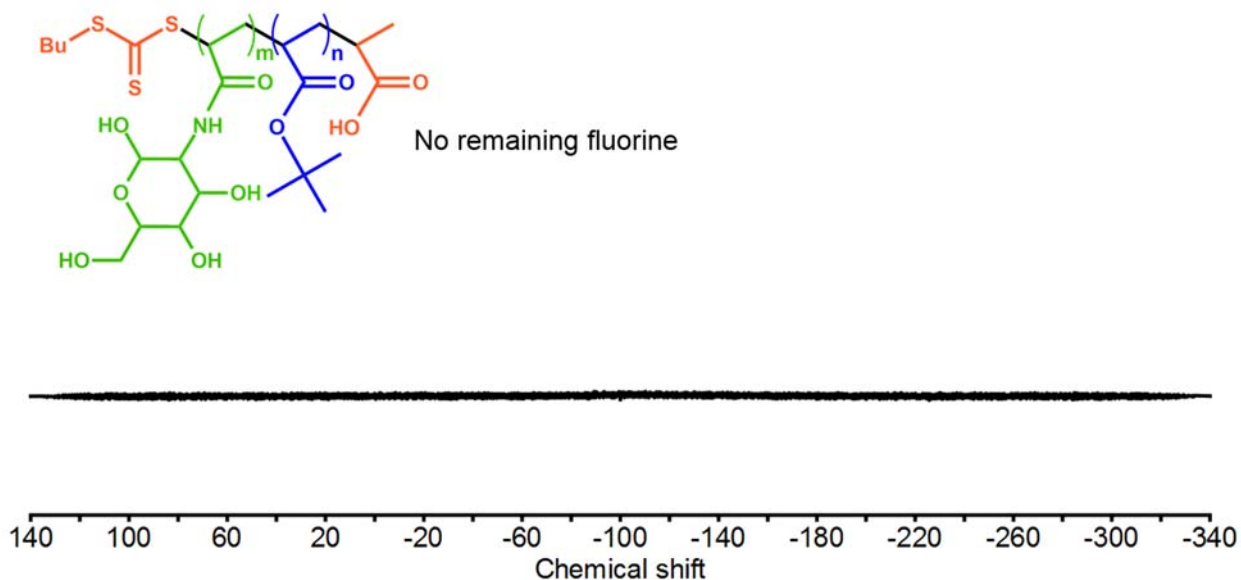


Figure S5. ^{19}F NMR spectrum of P(TBA-*b*-AGA) in $\text{DMSO-}d_6$.

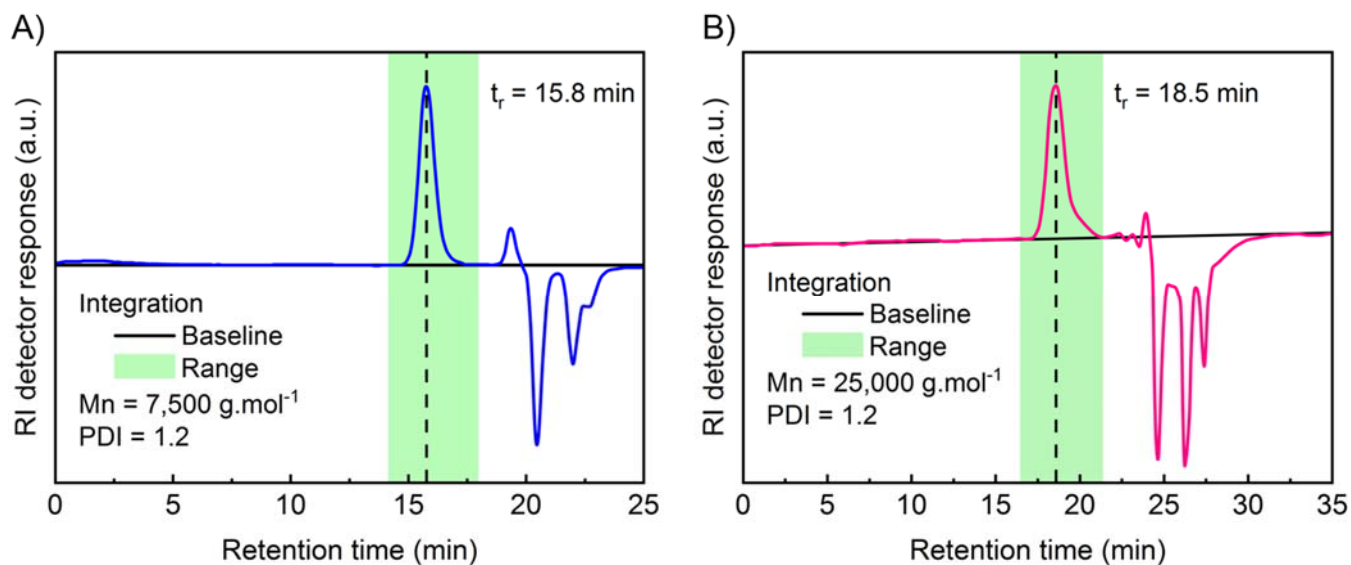


Figure S6. Size-exclusion chromatogram in THF: **(A)** P(TBA) homopolymer, **(B)** P(TBA-*b*-PFPA) diblock copolymer (eluent flow-rate = 0.4 mL.min $^{-1}$).

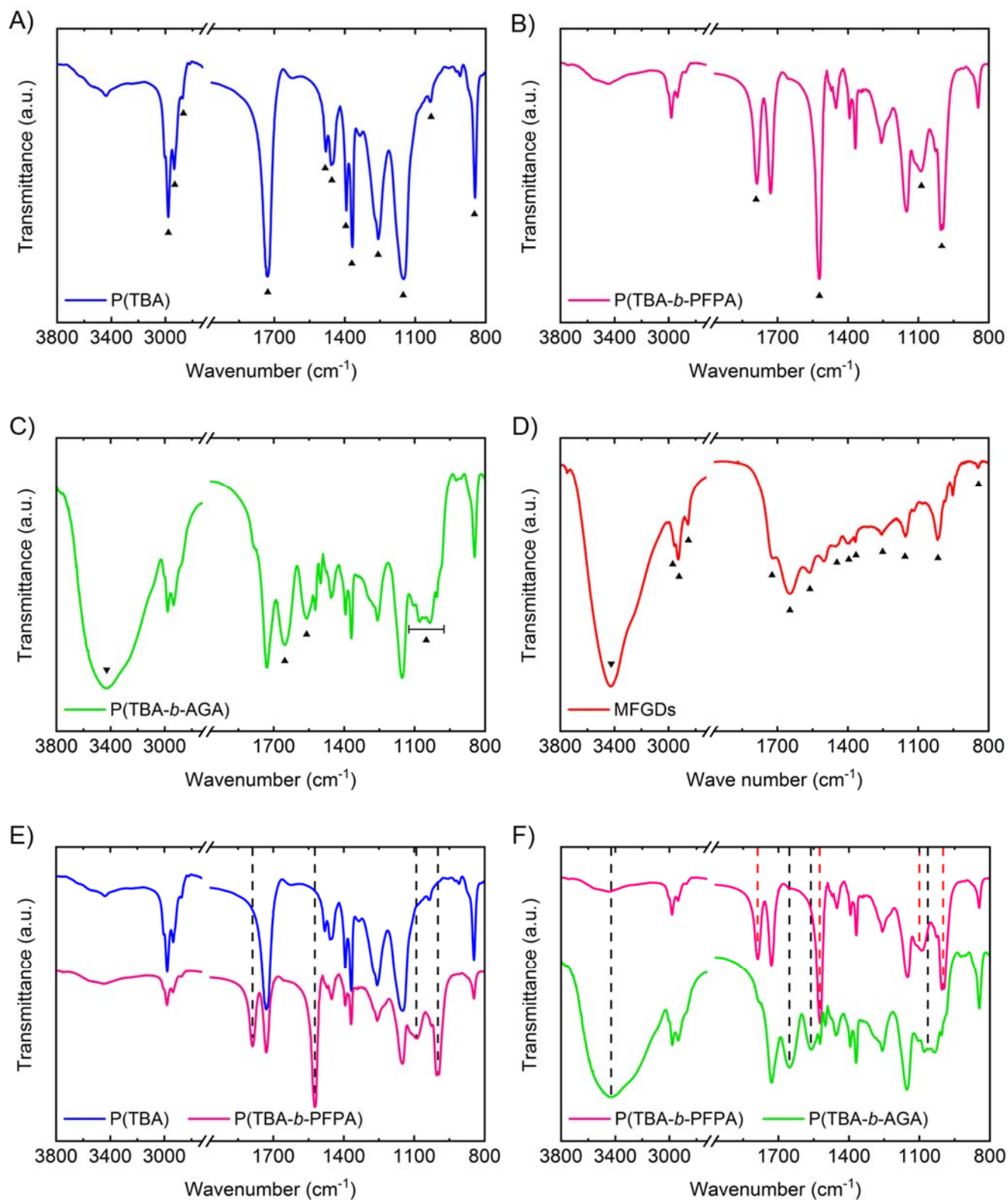


Figure S7. FTIR spectra (transmission): **(A)** P(TBA), **(B)** P(TBA-*b*-PFPA), **(C)** P(TBA-*b*-AGA), **(D)** MFGDs, **(E)** P(TBA) and P(TBA-*b*-PFPA) (stacked), **(F)** P(TBA-*b*-PFPA) and P(TBA-*b*-AGA) (stacked). Triangle symbols indicate bands reported in Table S1. Black (resp. red) dash lines indicate appearing (resp. disappearing) bands from a reacting polymer to the resulting one.

Table S1. FTIR bands assignment (from Figure S7) for the different polymeric blocks and the MFGDs.

	Wavenumber	Band attribution	Wavenumber	Band attribution
P(TBA) block	2980 cm ⁻¹	ν_{asym} (C-H) (<i>tert</i> -butyl)	1394 cm ⁻¹	δ (CH ₃) (<i>tert</i> -butyl)
	2935 cm ⁻¹	ν_{asym} (C-H) (<i>tert</i> -butyl)	1368 cm ⁻¹	δ (CH ₃) (<i>tert</i> -butyl)
	2875 cm ⁻¹	ν_{sym} (C-H) (<i>tert</i> -butyl)	1257 cm ⁻¹	ν (C- <i>tert</i> -butyl)
	1730 cm ⁻¹	ν (C=O)	1151 cm ⁻¹	ν (C-O)
	1481 cm ⁻¹	ρ (CH ₃) (<i>tert</i> -butyl)	1037 cm ⁻¹	γ (CH ₃) (<i>tert</i> -butyl)
	1458 cm ⁻¹	δ (CH ₂) (polymer backbone)	846 cm ⁻¹	γ (CH ₃) (<i>tert</i> -butyl)
P(PFPA) block	1789 cm ⁻¹	ν (C=O)	1090 cm ⁻¹	ν (C-O)
	1522 cm ⁻¹	ν (C=C)	1000 cm ⁻¹	ν (C-F)
P(AGA) block	3000-3700 cm ⁻¹	ν (O-H) ³	1561 cm ⁻¹	δ (N-H)
	1652 cm ⁻¹	ν (C=O) ³	975 - 1125 cm ⁻¹	ν (C-O) ³
MFGDs	3000-3700 cm ⁻¹	ν (O-H) (poly(acrylic acid))	1451 cm ⁻¹	δ (CH ₂) (poly(acrylic acid))
	2956 cm ⁻¹	ν (C-H) (poly(acrylic acid))	1394 cm ⁻¹	δ (CH ₃) (P(TBA)) (traces)
	2928 cm ⁻¹	ν (C-H) (poly(acrylic acid))	1368 cm ⁻¹	δ (CH ₃) (P(TBA)) (traces)
	2858 cm ⁻¹	ν (C-H) (poly(acrylic acid))	1256 cm ⁻¹	ν (C-O) (poly(acrylic acid))
	1718 cm ⁻¹	ν (C=O) (poly(acrylic acid))	1155 cm ⁻¹	ν (C-O) (poly(acrylic acid))
	1647 cm ⁻¹	ν (C=O) (amide II & III) (core)	1018 cm ⁻¹	ν (C-O) (MFGDs core))
	1565 cm ⁻¹	δ (N-H) (amide II) (core)	845 cm ⁻¹	γ (CH ₃) (P(TBA)) (traces)

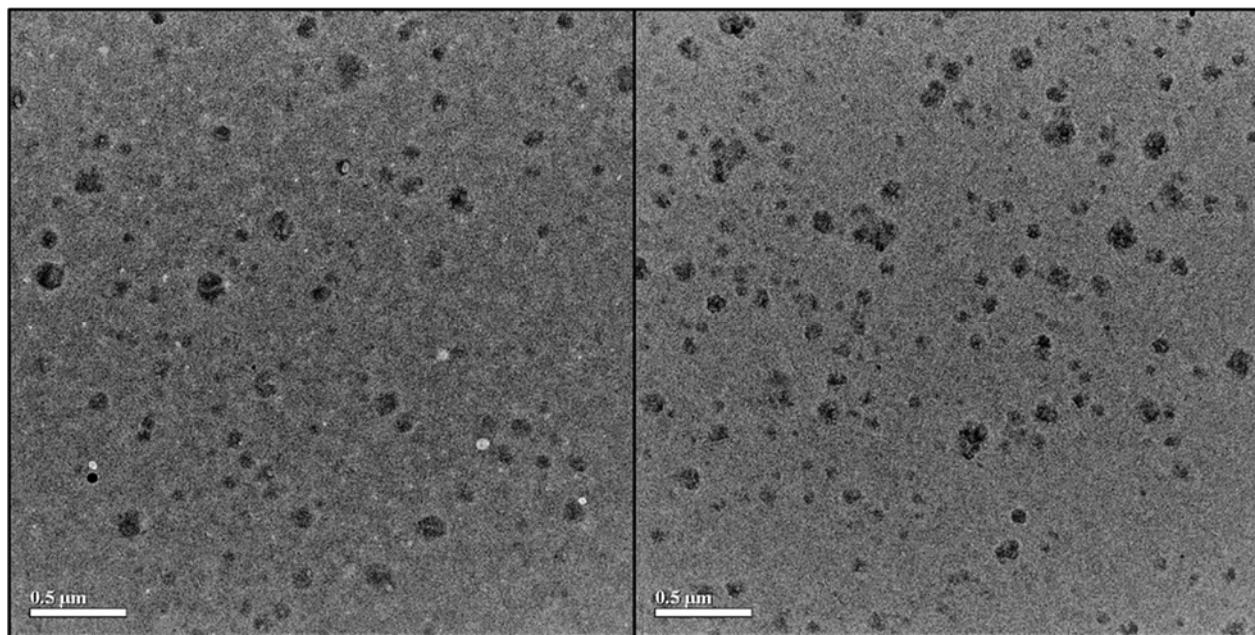


Figure S8. TEM images of P(TBA-*b*-AGA) reverse-micelles in a DMSO:1-heptanol (1:2, v:v) mixture. The white dots correspond to heterogeneities in the carbon Formvar supporting layer. Such heterogeneities are often observed when the grid is exposed to organic solvents (here DMSO and 1-heptanol).

Due to their dynamic nature, both size and morphology of the self-assembled polymeric micelles can change during TEM grid preparation. Therefore, TEM should only be used to confirm the presence of polymeric micelles, but not used to assess their size.

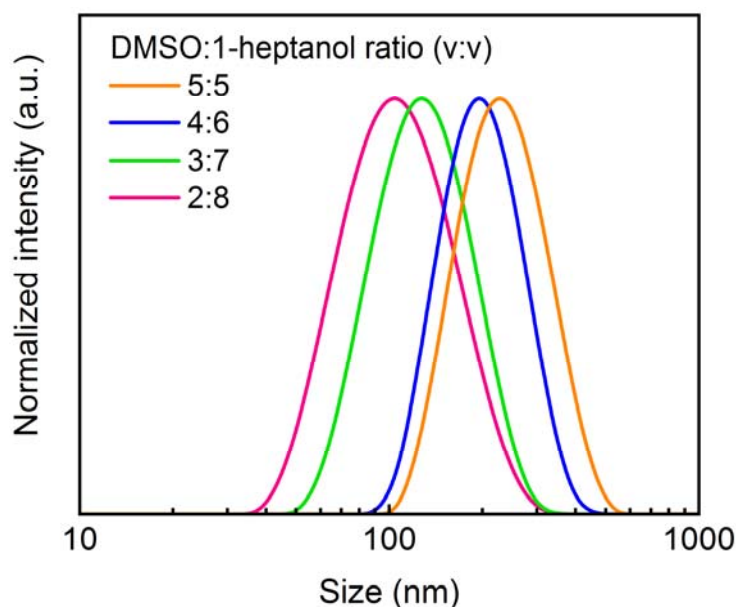


Figure S9. DLS size distributions (intensity) of P(TBA-*b*-AGA) reverse-micelles in various DMSO:1-heptanol mixtures.

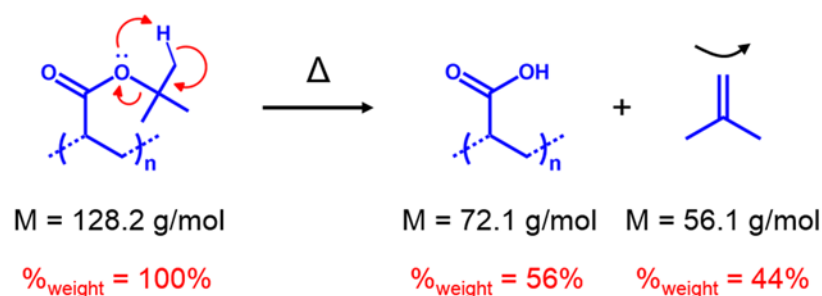
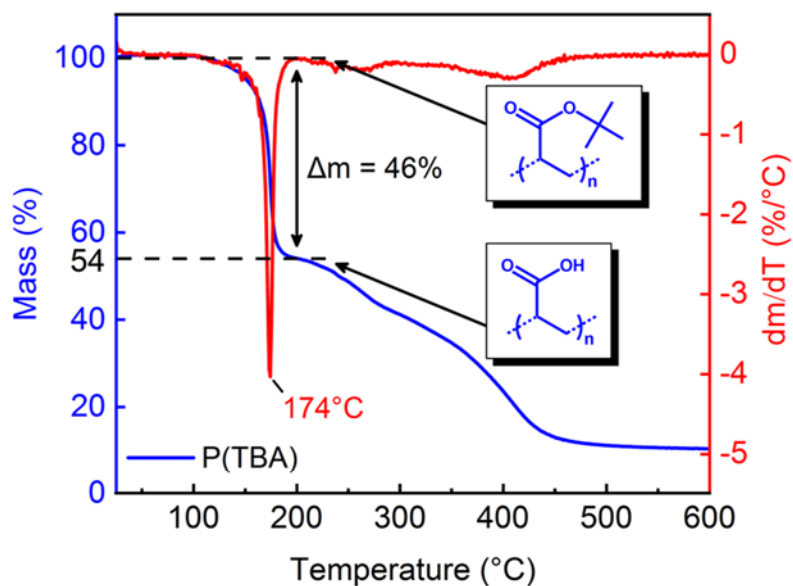


Figure S10. TGA curve of P(TBA). Results show a 46% mass loss, consistent with the conversion of the *tert*-butyl esters into carboxylic acid along the polymeric chain. Heating rate = 2°C.min⁻¹.

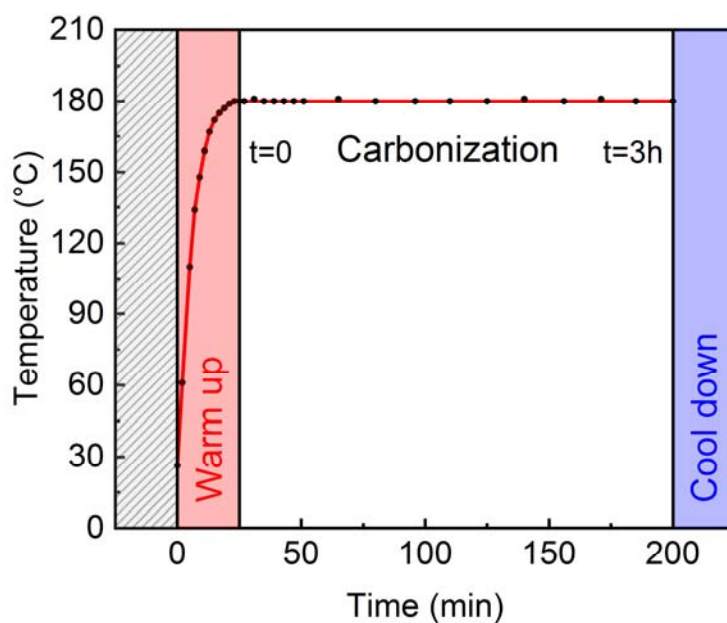


Figure S11. Temperature of the emulsion as a function of time during the graphitization step. Monitored in situ by dipping a temperature probe directly in the emulsion.

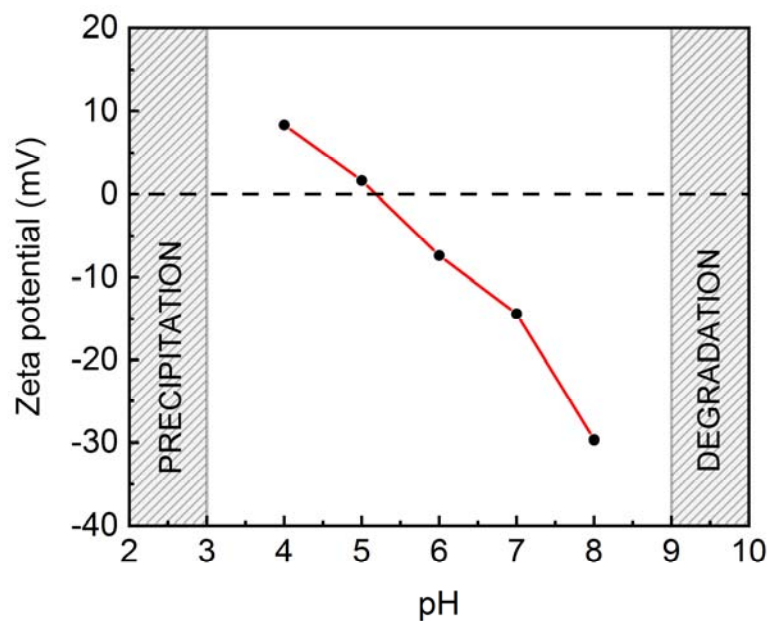


Figure S12. Zeta potential as a function of pH for MFGDs in various aqueous buffers.

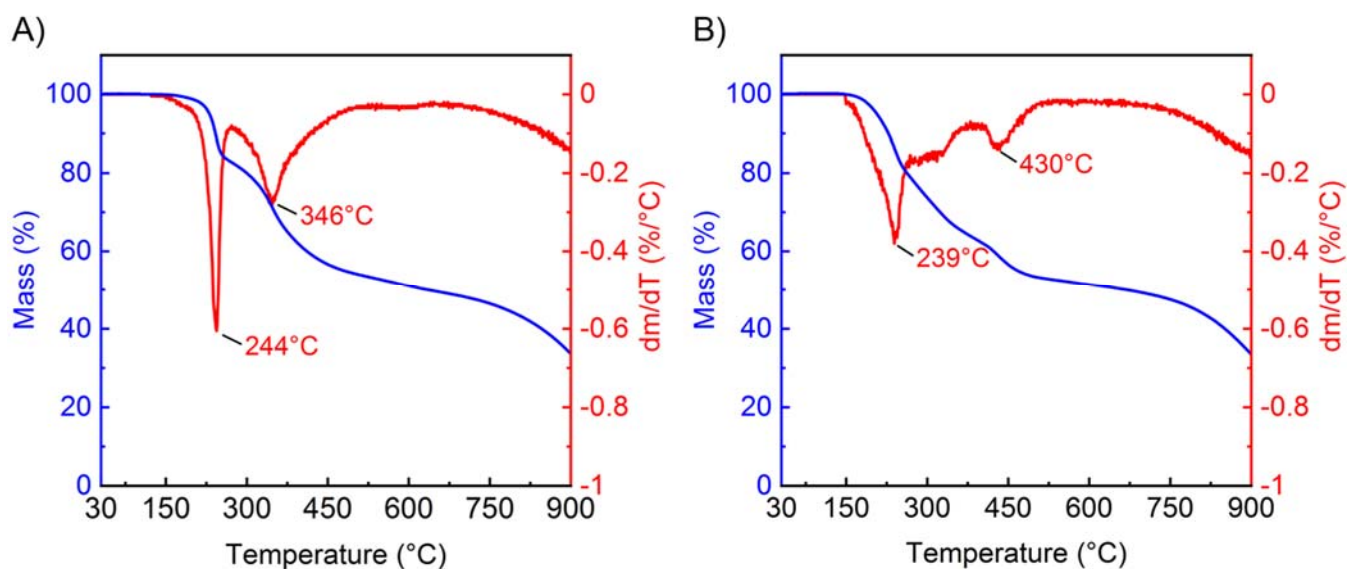


Figure S13. (A) TGA curve of raw MFGDs (recovered after graphitization, without purification). (B) TGA curve of purified MFGDs (redispersed in ethanol then centrifuged and filtered on 0.2 PTFE syringe filter, as detailed in the experimental section).

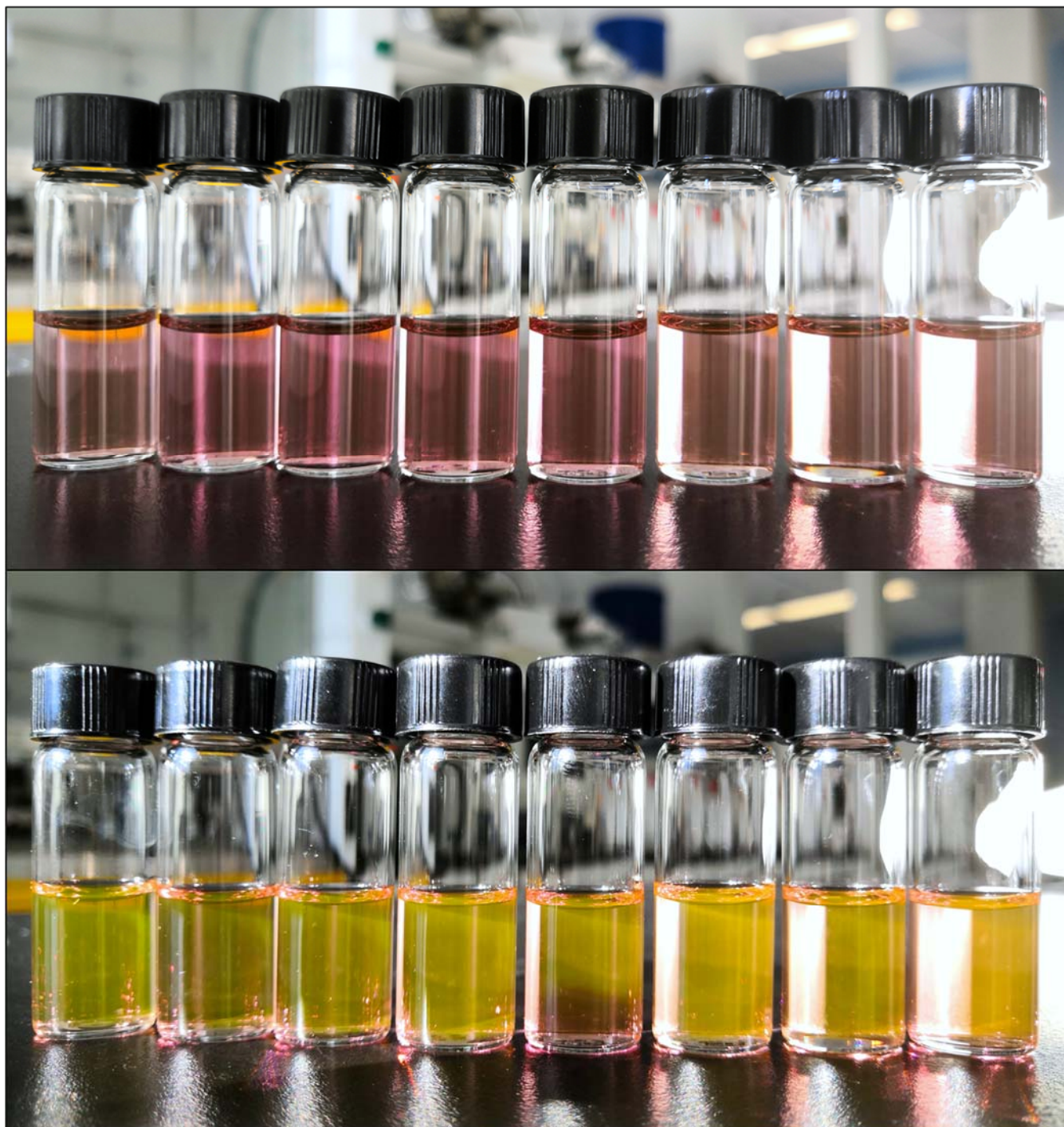


Figure S14. Photographs of MFGDs solutions in various solvents; from left to right: water, methanol, ethanol, isopropanol, 1-heptanol, dimethylformamide, dimethylsulfoxide, tetrahydrofuran. Vials shaded from the sun exhibiting a pink color (absorption) (upper row). Vials in sunlight exhibiting a yellow color (excitation then fluorescence) (lower row).

Since illumination conditions are not homogeneous within the picture, brightness should not be used as an indication of quantum yield. Notably we do not see any PL extinction phenomenon that would be expected if they were an actual interaction between the fluorophores and the solvent

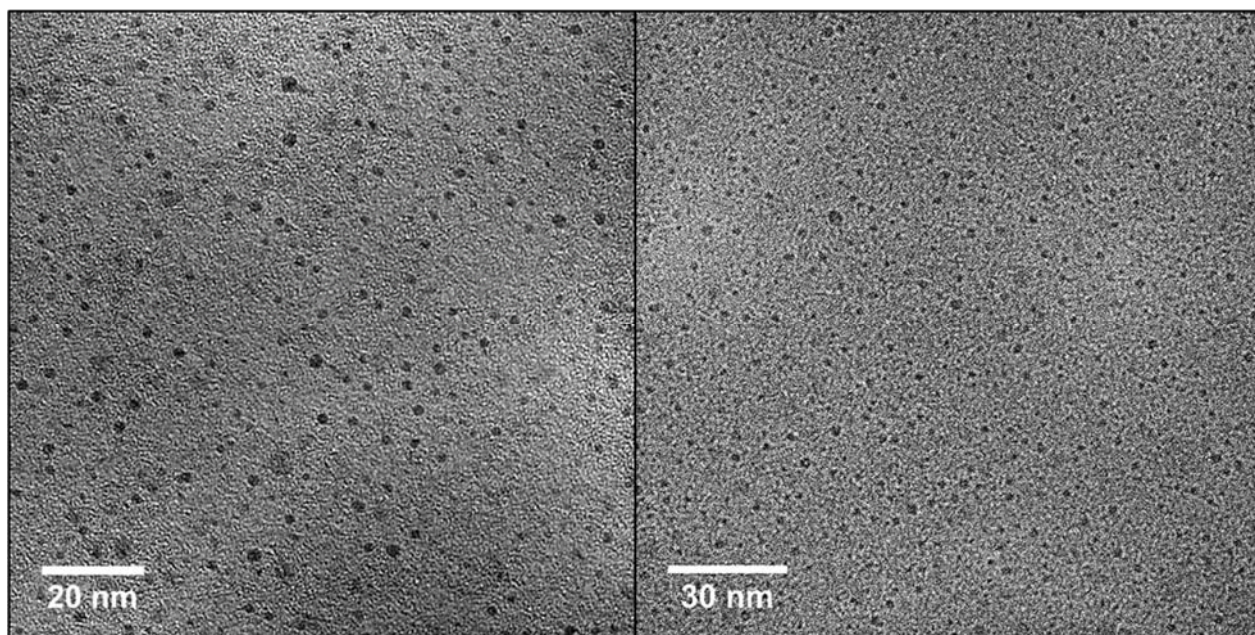


Figure S15. TEM images of dispersed MFGDs.

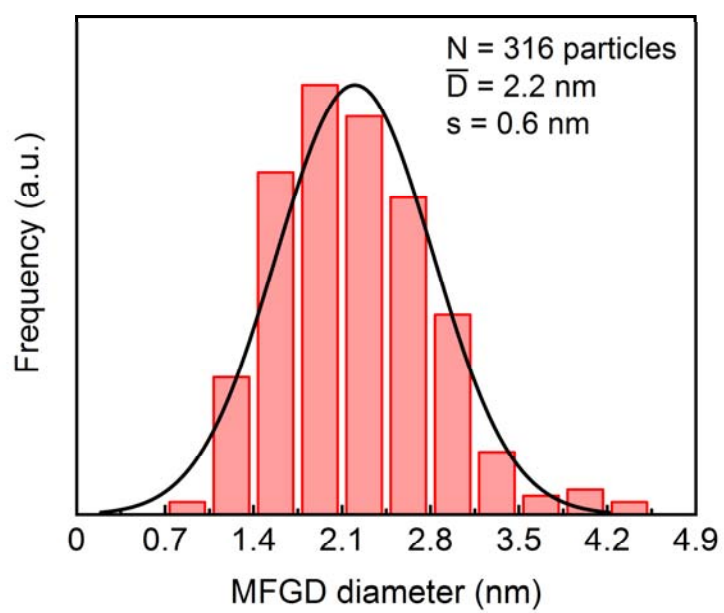


Figure S16. Size distribution histogram of MFGDs (from TEM images).

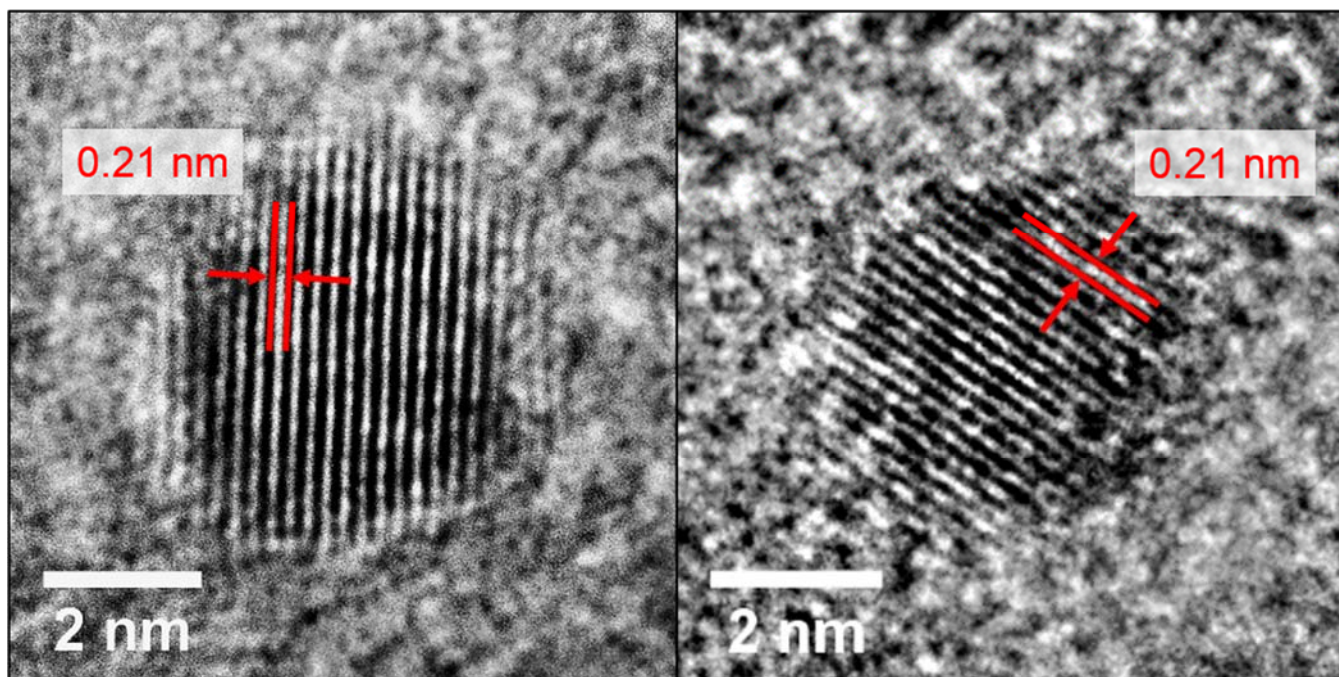


Figure S17. HR-TEM images of isolated MFGDs.

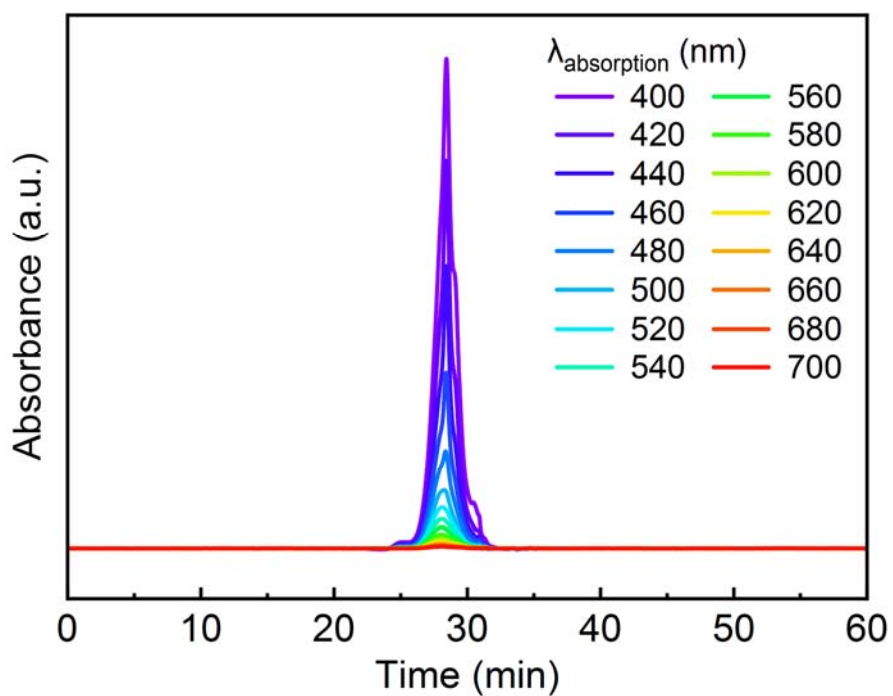


Figure S18. Size-exclusion chromatogram of MFGDs in THF (eluent flow-rate = 0.4 mL.min⁻¹). The chromatogram demonstrates that the optical properties come from a single species. Furthermore, its elution time corresponds to a nanosized object and not to a low-molecular weight molecule.

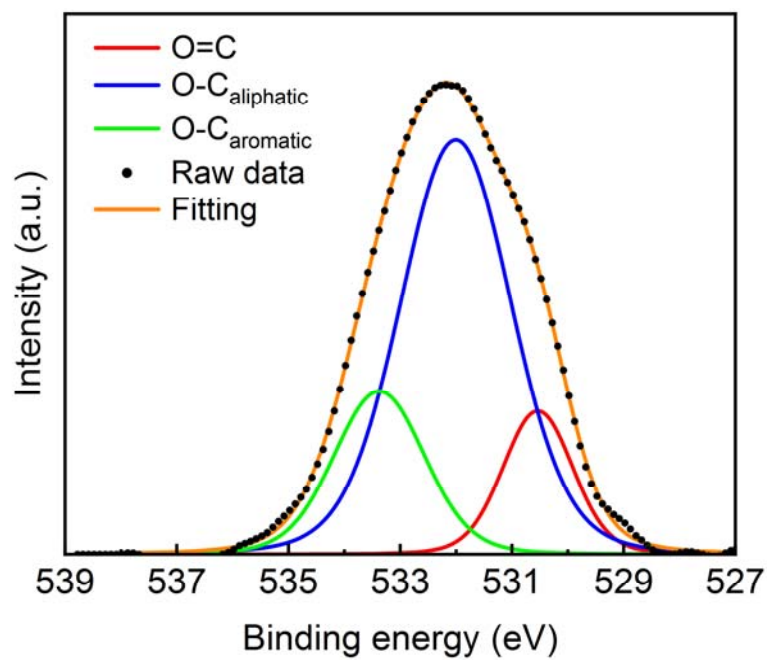


Figure S19. O1s XPS spectrum of MFGDs.

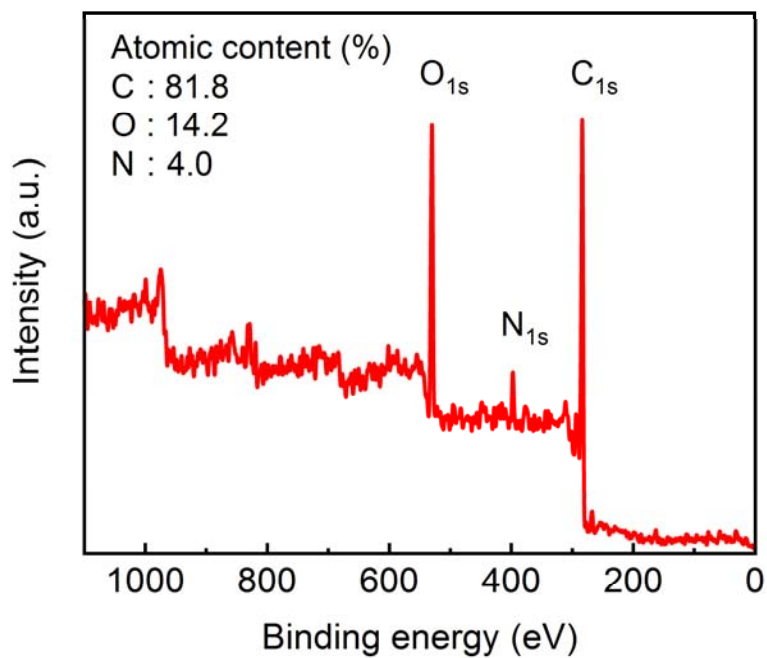
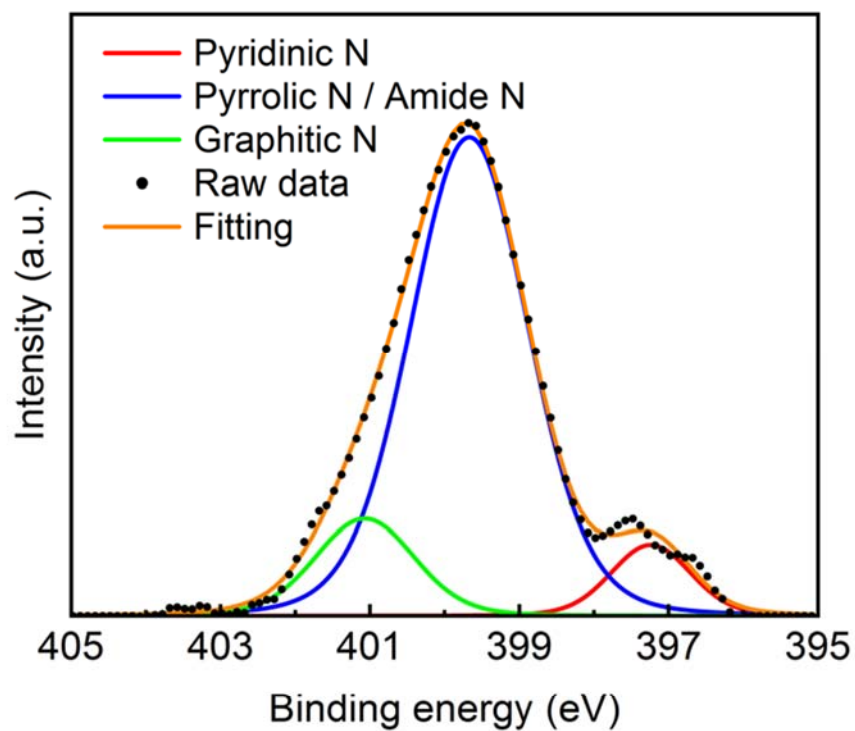
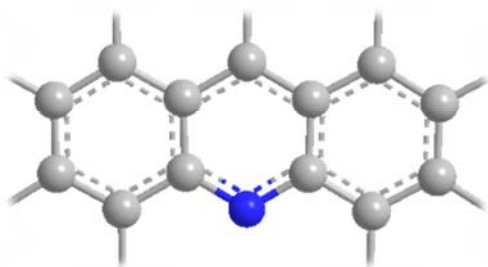


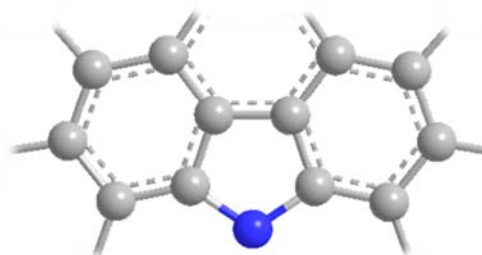
Figure S20. Survey XPS spectrum of MFGDs.



Carbon
 Nitrogen
 Oxygen



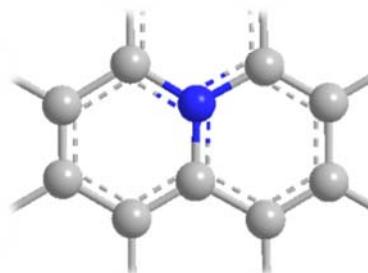
Pyridinic N



Pyrrolic N



Amide N



Graphitic N

Figure S21. N1s XPS spectrum of MFGDs.

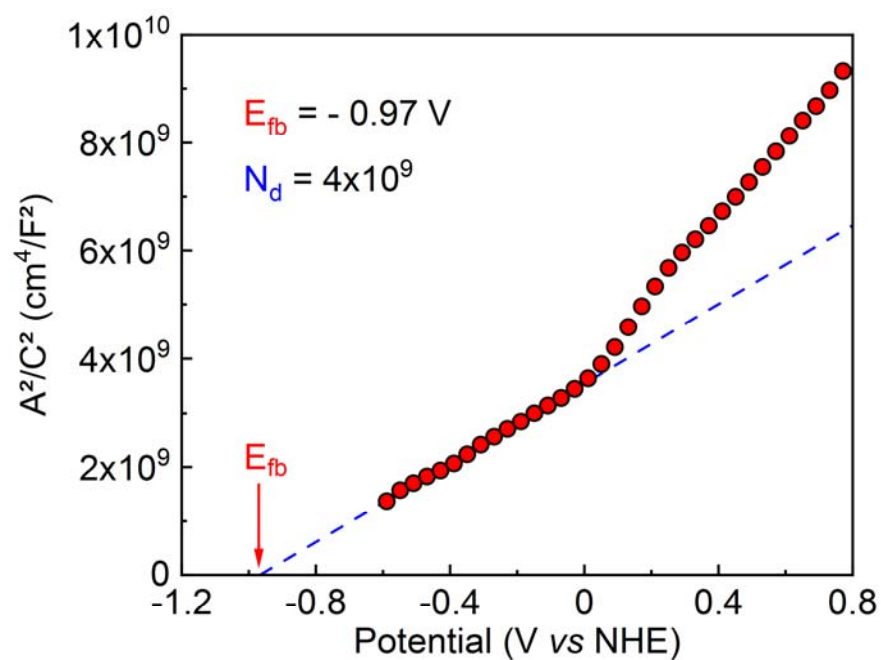


Figure S22. Mott-Schottky plot for MFGDs dropcasted on FTO and immersed in 0.5 M Na_2SO_4 at pH = 7



Figure S23. Photographs of dried MFGDs appearing as a dark brick-red fine powder (from 2 different batches). White dots are shining facets of some of the powdered particles.

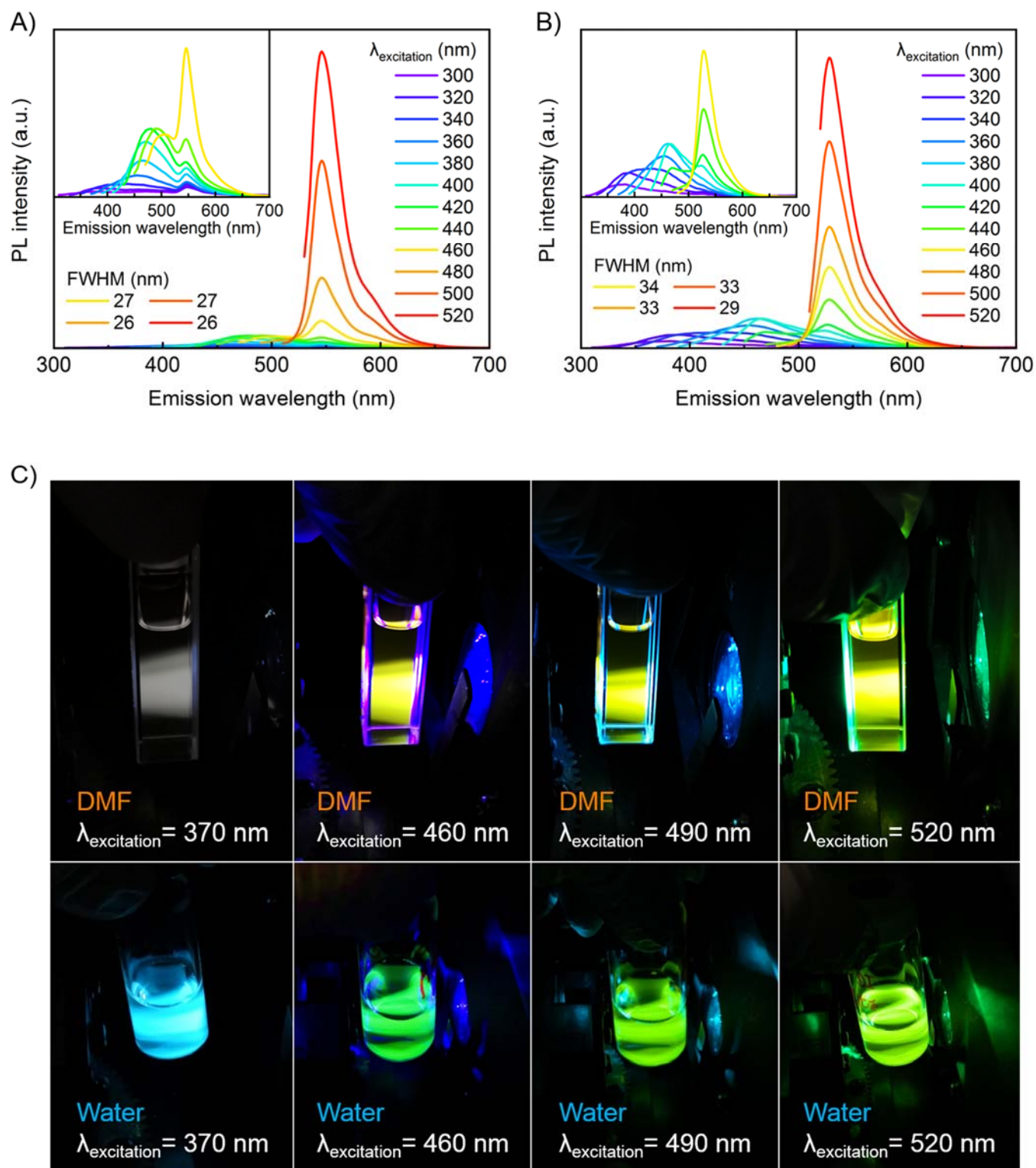


Figure S24. PL spectra of MFGDs at various excitation wavelengths: (A) in DMF, (B) in nanopure water. Insets: zoom of the PL spectra at low excitation wavelength (300–460 nm). (C) Photographs of MFGDs under selected excitation wavelengths: in DMF (upper row), in nanopure water (lower row).

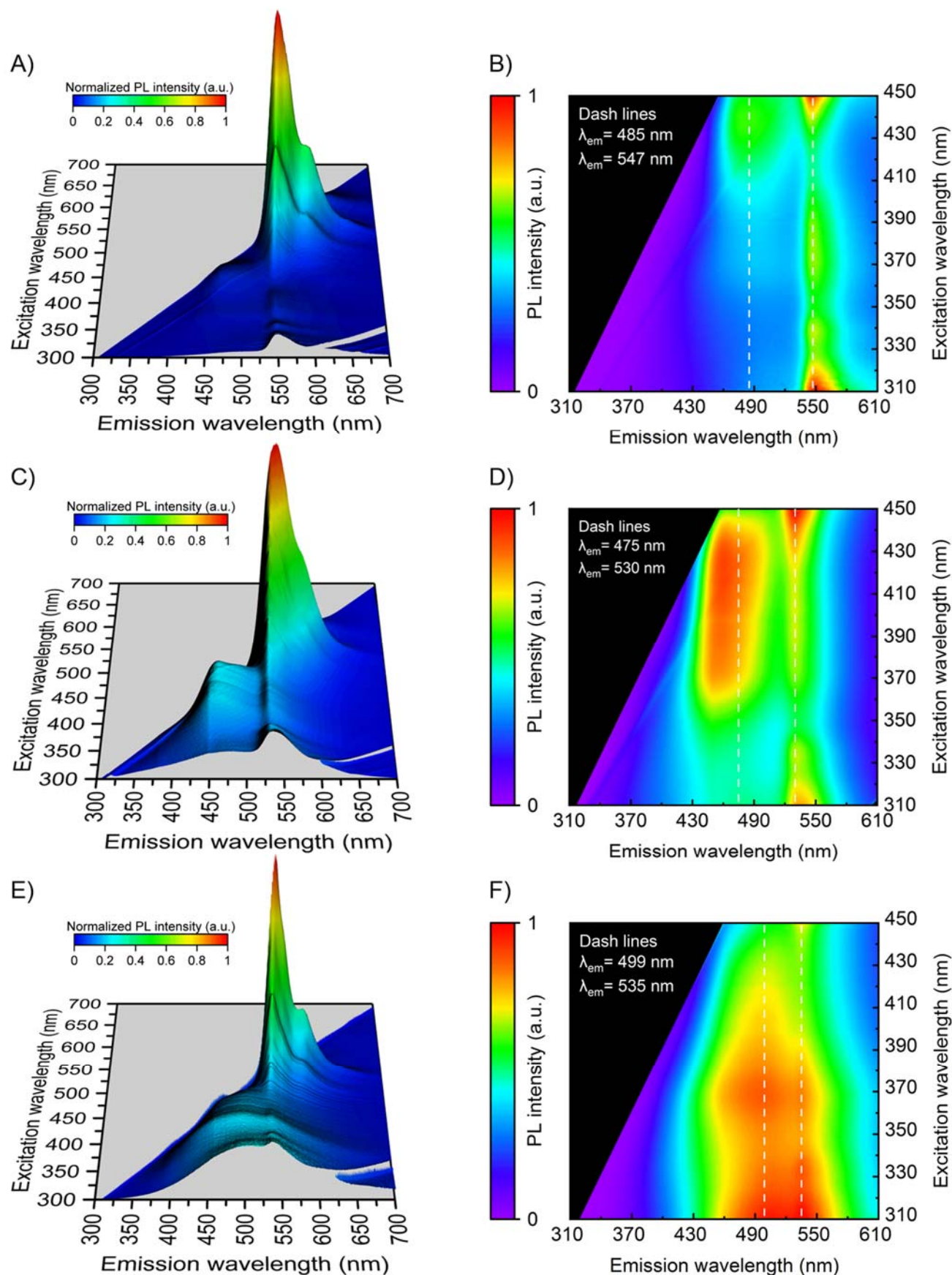


Figure S25. (A) PL map of MFGDs in solution in DMF and (B) associated zoom in the range $\lambda_{excitation} = 310$ -450 nm. (C) PL map of MFGDs in solution in water and (D) associated zoom in the range $\lambda_{excitation} = 310$ -450 nm. (E) PL map of MFGDs dispersed in a PVDF film and (F) associated zoom in the range $\lambda_{excitation} = 310$ -450 nm.

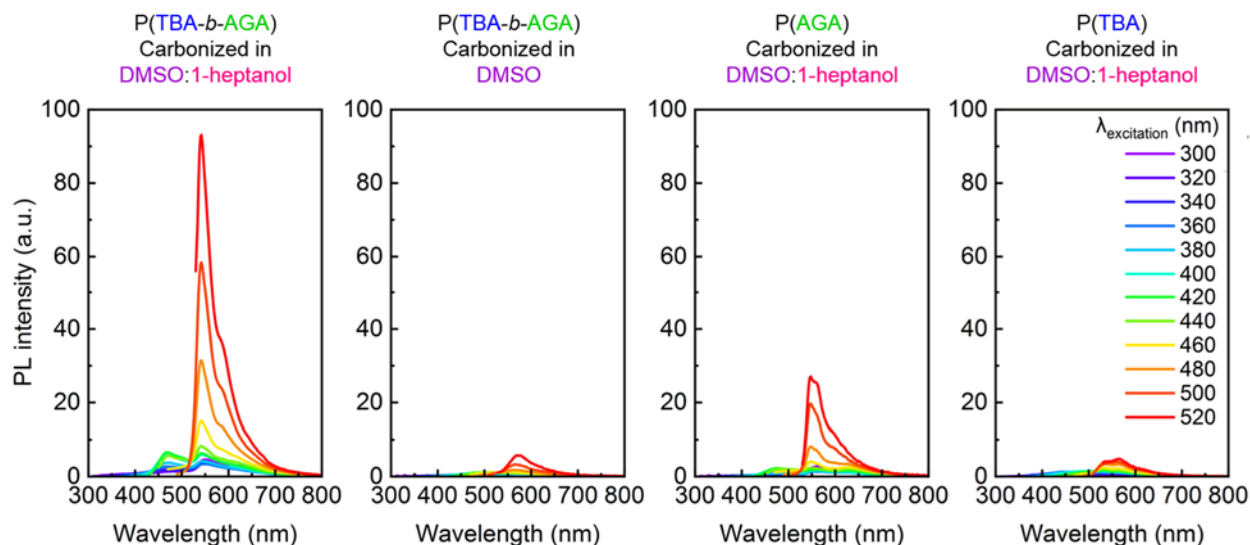


Figure S26. PL spectra in DMF from graphitization control experiments using different precursors or solvents:

- 1) P(TBA-*b*-AGA) in DMSO:1-heptanol → + stabilizing block + graphitizing block + self-assembly (→ MFGDs)
- 2) P(TBA-*b*-AGA) in DMSO → + stabilizing block + graphitizing block - self-assembly
- 3) P(AGA) in DMSO:1-heptanol → + graphitizing block - stabilizing block - self-assembly
- 4) P(TBA) in DMSO:1-heptanol → + stabilizing block - graphitizing block - self-assembly

All graphitizations were done with identical mass of precursor (90 mg) and volume of solvent(s) (15 mL) at 180°C for 3h. Resulting residues were dissolved in identical amount of DMF, centrifuged, filtered on 0.2µm PTFE then diluted in identical amount of DMF prior to PL measurement. The 4 presented PL spectra thus share the same Y-axis scale. It is clear from these PL intensities that the graphitization of P(TBA-*b*-AGA) in DMSO:1-heptanol is the only route able to provide MFGDs quantitatively.

More precisely, these spectra demonstrate that the self-assembly step prior to graphitization is responsible for the specific photophysical properties of the MFGDs (experiment 1 vs. experiments 2,3 and 4). The PL results also confirm that the self-assembly relies on the nature of both the precursor and the medium involved *i.e.* a diblock copolymer and a solvents binary mixture are necessary (experiment 1). Indeed, no self-assembly of homopolymers is observed in DMSO:1-heptanol (experiments 3 and 4) and no self-assembly of the diblock copolymer occurs in pure DMSO (experiment 2).

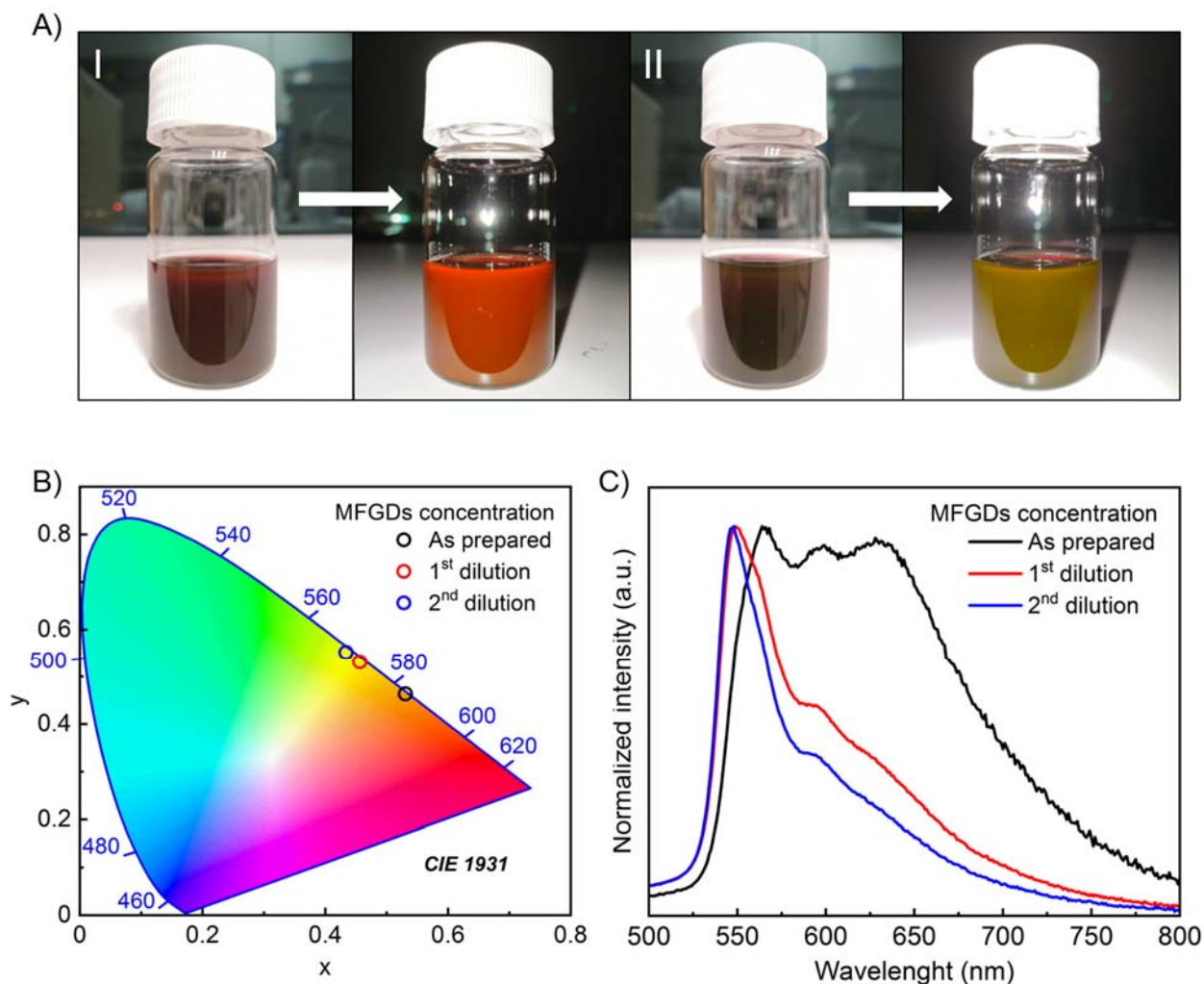


Figure S27. (A) Photographs of MFGDs at different concentration in DMF ($C_I > C_{II}$), under ambient light (left) and under a white LED excitation (right). (B) CIE 1931 chromaticity diagram: emission color of MFGDs in DMF as a function of their concentration. (C) PL spectra of MFGDs in DMF ($\lambda_{\text{excitation}} = 470 \text{ nm}$) with varying concentration.

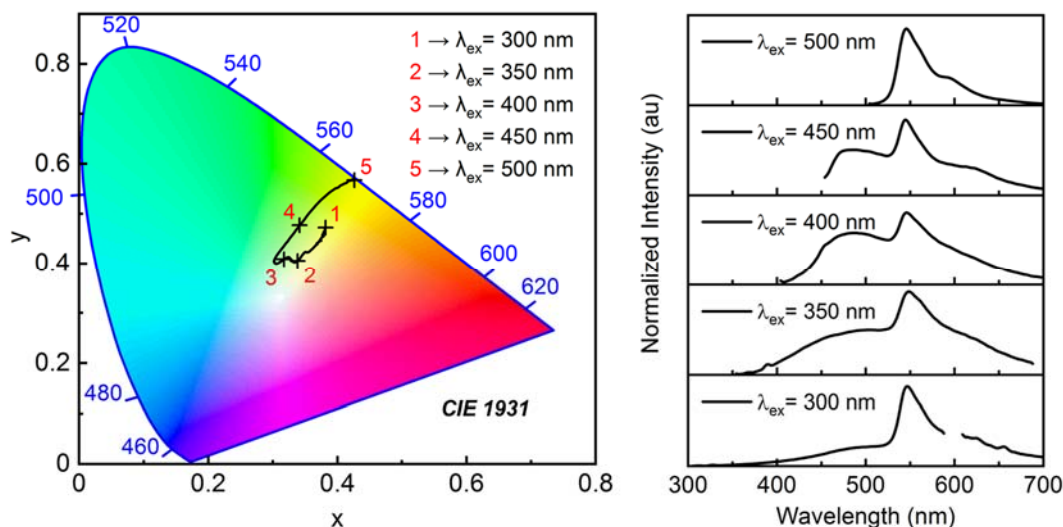


Figure S28. CIE 1931 chromaticity diagram: emission color of MFGDs in DMF as a function of the excitation wavelength (left). Corresponding PL spectra (right).

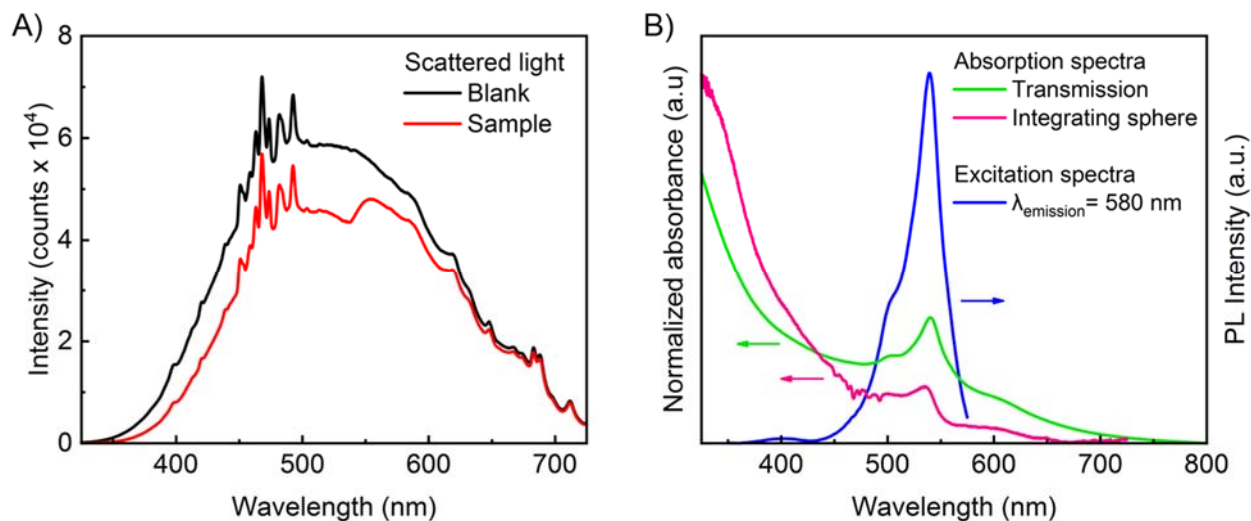


Figure S29. (A) Scattered light intensity as a function of wavelength from MFGDs in DMF (in red) and from the blank (in black). (B) Corresponding calculated UV-vis absorption spectrum ($A = -\log(I_{\text{sample}}/I_{\text{blank}}$, in pink), transmission-measured UV-vis absorption spectrum (in green), excitation spectrum (in blue).

To confirm that the differences between the measured absorption and excitation spectrum were not due to the diffusion of light (from particles in suspension) the absorption spectrum was measured by irradiating a sample and blank with a zero-order excitation (white light) from a xenon lamp and measuring the intensity of the scattered light inside an integrating sphere. From the scattered light intensities from the blank and from the sample, the absorption spectrum can be reconstructed to obtain a spectrum that is not be obscured by scattering (Figure S27B, pink curve)

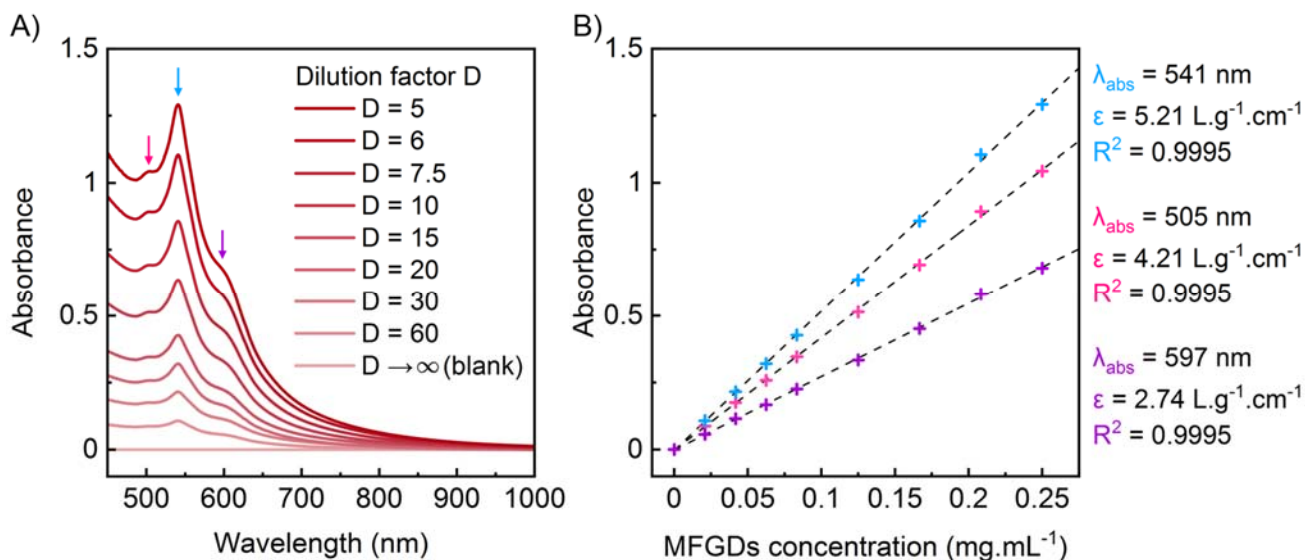


Figure S30. (A) UV-vis absorption spectra of MFGDs in solution in DMF at various dilution. Arrows are pointing at bands that are used for the linear regressions on Fig. S28 B. (B) Beer-Lambert plot from associated UV-vis absorption spectra. (C) Conversion table between mass attenuation coefficient and molar attenuation coefficient.

Molar ϵ calculation from Mass ϵ requires the following assumptions:

- MFGDs are regarded as a simple graphene oxide sphere of volume V.
- MFGDs have a density of $\rho \sim 1.8 \text{ g.cm}^{-3}$ (graphene oxide), intermediate between the density of graphite ($\rho \sim 2.2 \text{ g.cm}^{-3}$) and the density of poly(acrylic acid) ($\rho \sim 1.4 \text{ g.cm}^{-3}$).
- MFGDs have a mean radius of $R = 1.1 \text{ nm}$ (as determined via TEM, Figures S15-S16).

Molar ϵ can be calculated from the following equation:

$$\epsilon_{molar} = \rho V N_A \epsilon_{mass} \quad (5)$$

Where N_A is the Avogadro constant. Equation (5) can be rewritten in the case of a sphere as:

$$\epsilon_{molar} = \rho \frac{4}{3} \pi R^3 N_A \epsilon_{mass} \quad (6)$$

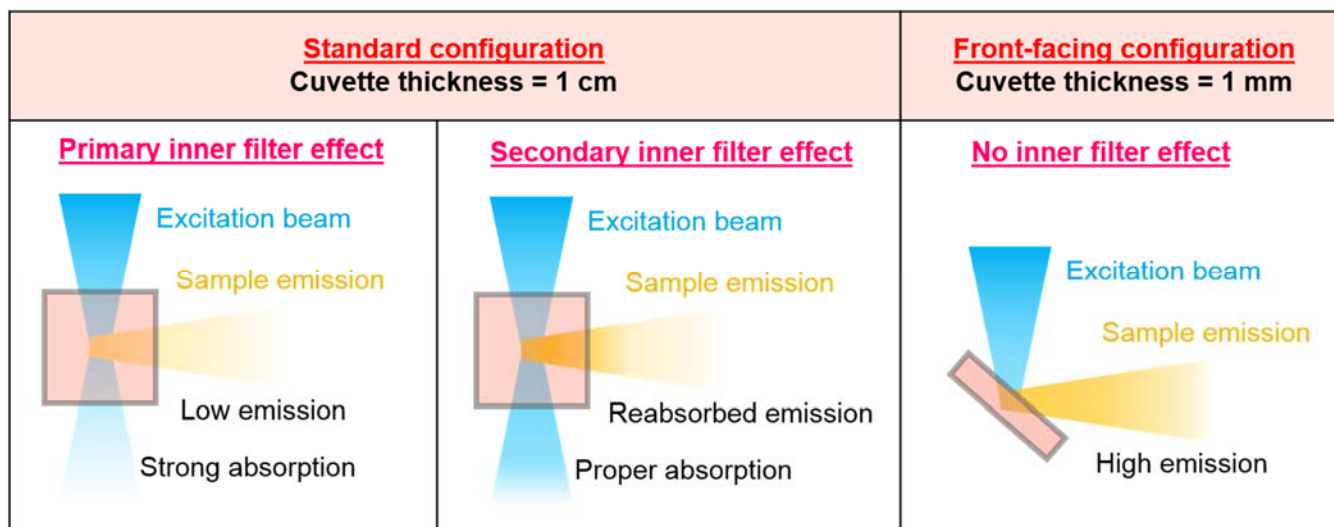


Figure S31. Schematic representation of a “standard” and a “front-facing” configurations for PL measurement. Schematic representation of the corresponding and classically encountered filter effects.

Primary inner filter effect: when a sample is too absorptive (overconcentrated and/or species with high molar attenuation coefficient) so that the excitation light cannot go through and the subsequent low emission cannot reach the photon detector quantitatively.

Secondary inner filter effect: when a sample shows a significant overlap of the excitation and emission spectra, then the light emitted from the center of the cuvette can be partially reabsorbed by the sample itself resulting in either low emission intensity or apparent change (shifts) in the measured emission spectrum.

Front-facing configuration: the smaller optical path in the cuvette mitigates the excitation light absorption and ensures low reabsorption of the fluoresced photons.

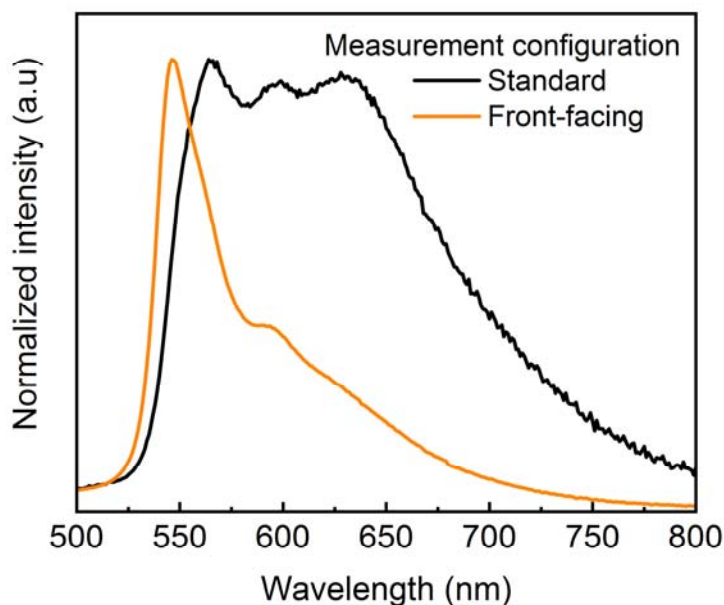


Figure S32. PL spectra of concentrated (as-prepared) MFGDs in DMF, using a “standard” and a “front-facing” configuration at $\lambda_{\text{excitation}} = 470$ nm. Configurations are described further on Figure S31.

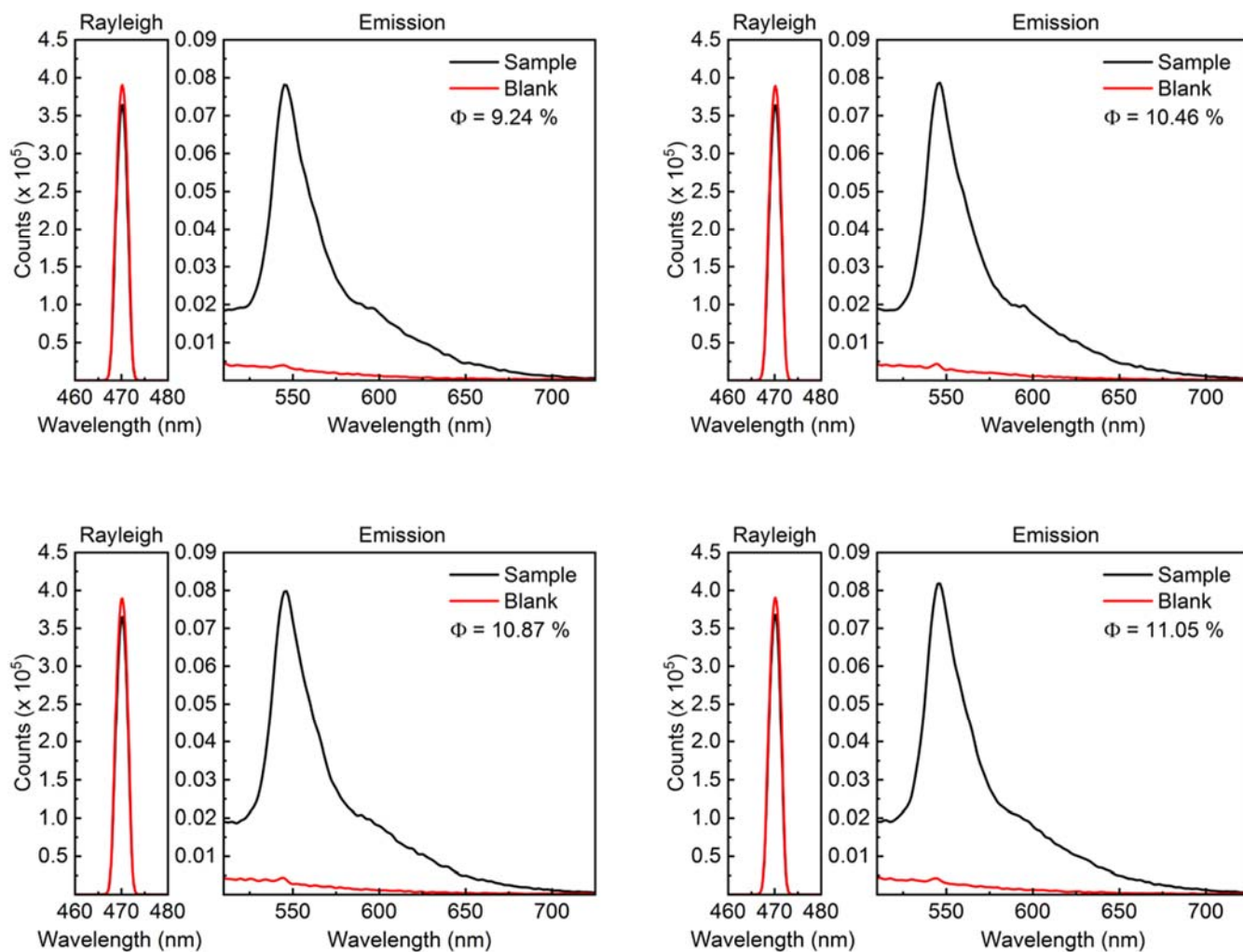


Figure S33. Quantum yield measurements of MFGDs in DMF made from a Quanta-φ integrating sphere with a 470 nm excitation. Average quantum yield = $10.4 \pm 0.8\%$

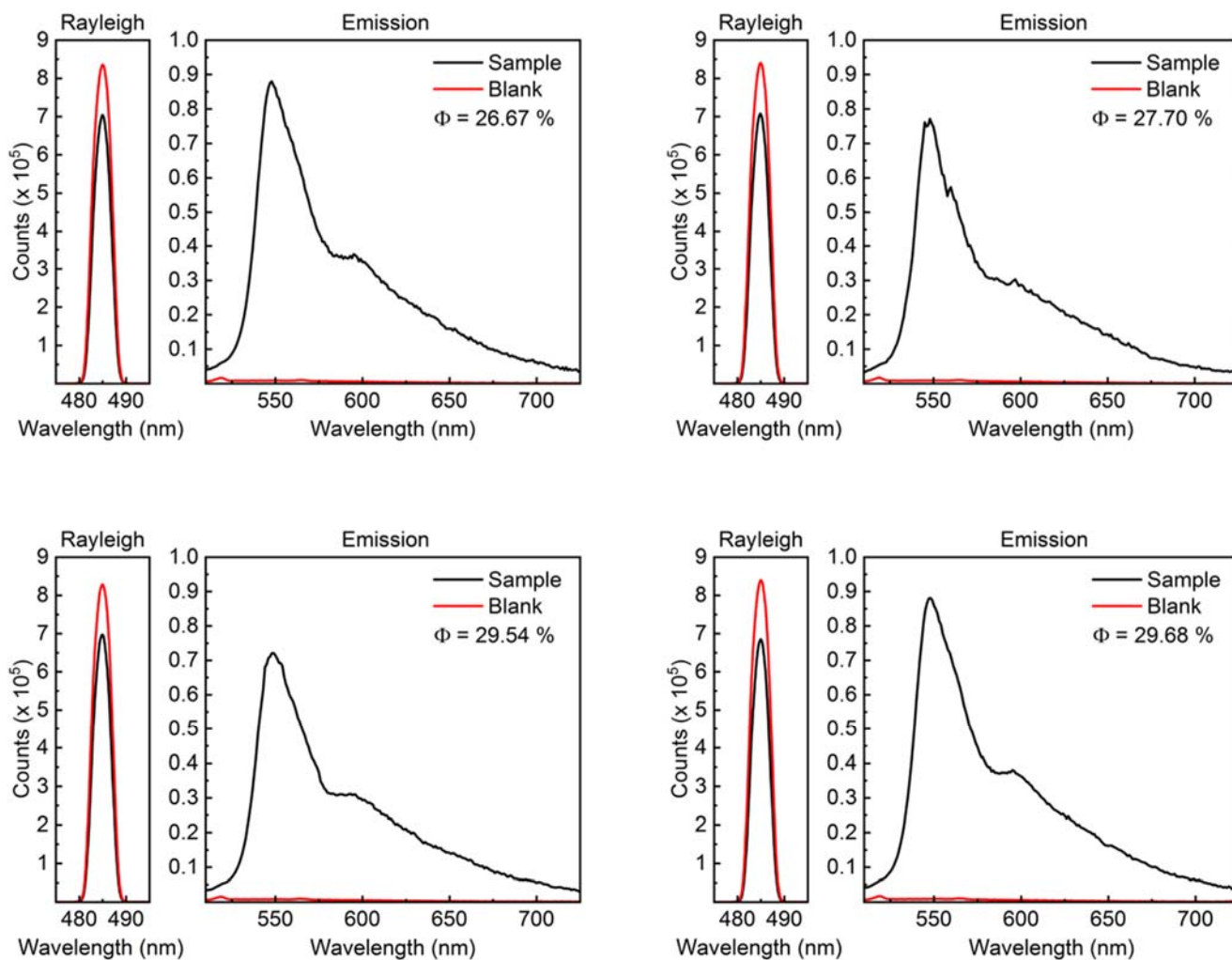


Figure S34. Quantum yield measurements of MFGDs in DMF made from a Quanta-φ integrating sphere with a 485 nm excitation. Average quantum yield = $28.4 \pm 1.5\%$

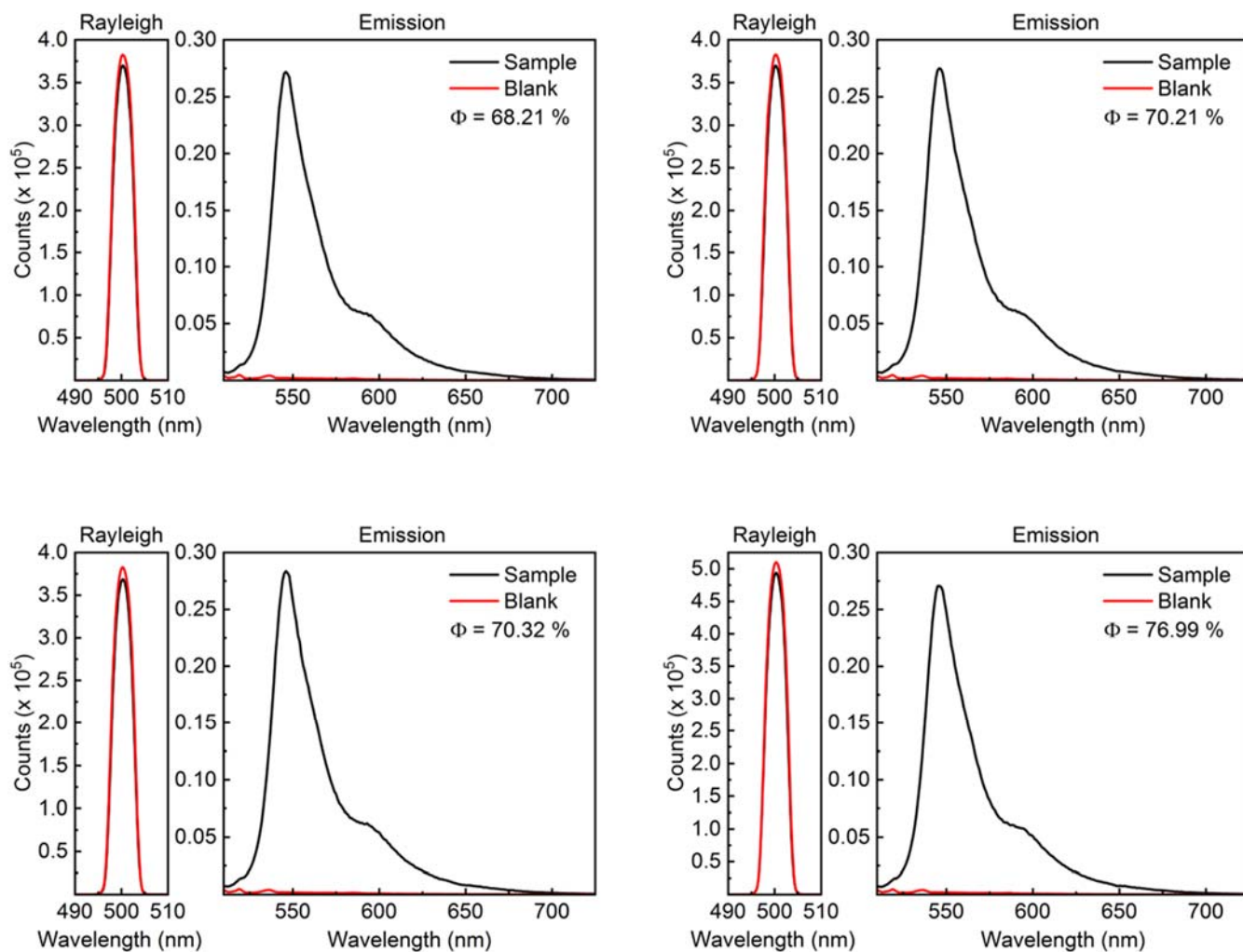


Figure S35. Quantum yield measurements of MFGDs in DMF made from a Quanta-φ integrating sphere with a 500 nm excitation. Average quantum yield = $71.4 \pm 3.8\%$.

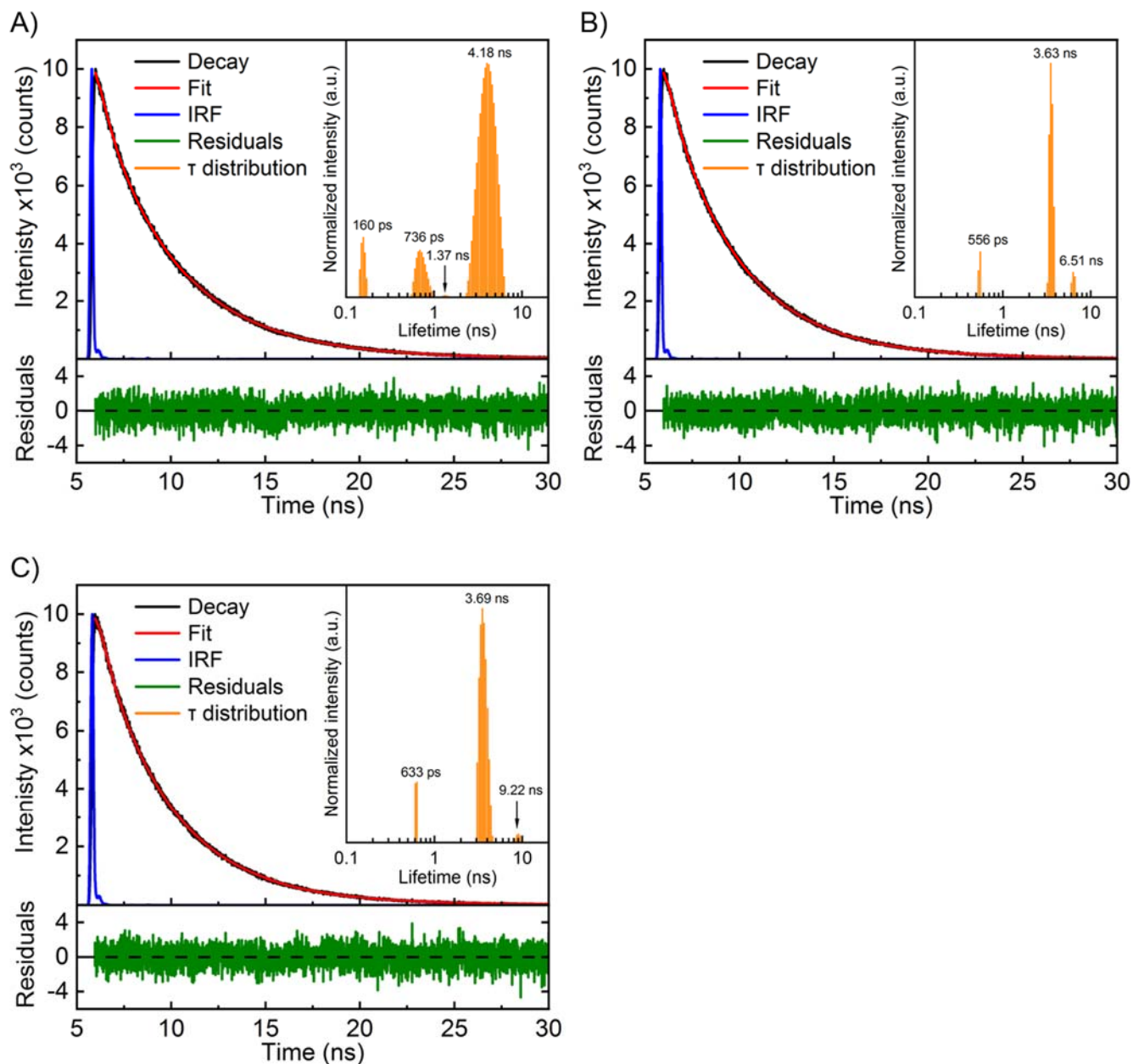


Figure S36. TCSPC decay traces, fits, lifetime distributions - MFGDs in DMF at different concentrations (from highest to lowest from A to C) ($\lambda_{\text{ex}} = 477 \text{ nm}$, $\lambda_{\text{em}} = 547 \text{ nm}$). Inset: corresponding distribution analysis fit.

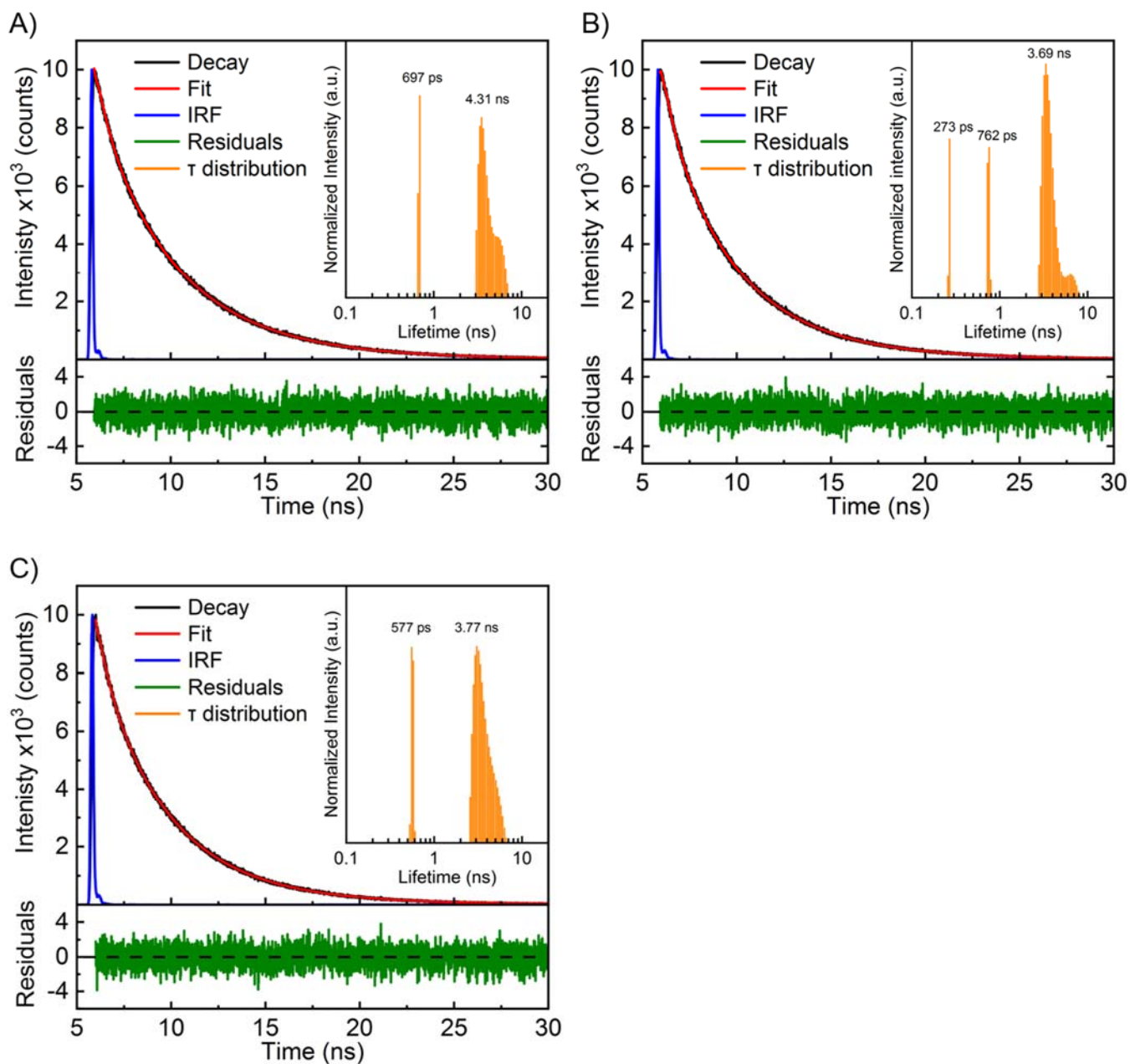


Figure S37. TCSPC decay traces, fits, lifetime distributions - MFGDs in DMF at different concentrations (from highest to lowest from A to C) ($\lambda_{\text{ex}} = 477 \text{ nm}$, $\lambda_{\text{em}} = 598 \text{ nm}$). Inset: corresponding distribution analysis fit.

Table S2. PL lifetime fits (distribution analysis) - MFGDs in DMF ($\lambda_{\text{ex}} = 477$ nm, $\lambda_{\text{em}} = 547$ nm).

Concentration	B ^a	f (%) ^b	τ^c	T ^d	$\langle \tau \rangle^e$	χ^2
As prepared	2.1×10^{-3}	0.2	159 ± 9 ps ^f	160 ps	3.93 ns	1.079
	3.7×10^{-3}	2.0	708 ± 94 ps	708 ps		
	6.4×10^{-5}	0.1	1.37 ± 0.08 ns	1.39 ns		
	3.1×10^{-2}	97.7	4.18 ± 0.88 ns	4.10 ns		
First dilution	3.2×10^{-3}	1.3	556 ± 14 ps	565 ps	3.99 ns	1.067
	3.0×10^{-2}	84.5	3.63 ± 0.18 ns	3.58 ns		
	2.8×10^{-3}	14.2	6.51 ± 0.27 ns	6.44 ns		
Second dilution	2.8×10^{-3}	1.5	633 ± 16 ps	647 ps	3.93 ns	1.081
	3.2×10^{-2}	93.5	3.69 ± 0.35 ns	3.58 ns		
	7.0×10^{-4}	5.0	9.22 ± 0.51 ns	9.23 ns		

- a) Pre-exponential factor
b) Fluorescence intensity percentage
c) Center of gravity of the distribution spike
d) Maximum of the distribution spike
e) Average lifetime $\langle \tau \rangle = \sum_{i=1}^n B_i \tau_i^2 / \sum_{i=1}^n B_i \tau_i$
f) Unreliable lifetime considering the IRF FWHM (175 ps)

Table S3. PL lifetime fits (distribution analysis) - MFGDs in DMF ($\lambda_{\text{ex}} = 477$ nm, $\lambda_{\text{em}} = 598$ nm).

Concentration	B ^a	f (%) ^b	τ^c	T ^d	$\langle \tau \rangle^e$	χ^2
As prepared	5.6×10^{-2}	0.3	7 ± 1 ps ^f	7 ps	4.18 ns	1.085
	7.4×10^{-3}	0.4	76 ± 2 ps ^f	74 ps		
	5.5×10^{-3}	2.8	697 ± 17 ps	708 ps		
	3.0×10^{-2}	96.5	4.31 ± 0.98 ns	3.58 ns		
First dilution	2.7×10^{-3}	0.6	273 ± 5 ps ^f	275 ps	3.98 ns	1.071
	4.6×10^{-3}	2.9	762 ± 23 ps	775 ps		
	2.7×10^{-2}	82.8	3.69 ± 0.54 ns	3.43 ns		
	2.5×10^{-3}	13.7	6.62 ± 0.71 ns	6.44 ns		
Second dilution	2.9×10^{-2}	1.0	43 ± 1 ps ^f	43 ps	3.64 ns	1.081
	5.6×10^{-3}	2.7	577 ± 18 ps	565 ps		
	3.0×10^{-2}	96.3	3.77 ± 0.89 ns	3.13 ns		

- a) Pre-exponential factor
b) Fluorescence intensity percentage
c) Center of gravity of the distribution spike
d) Maximum of the distribution spike
e) Average lifetime $\langle \tau \rangle = \sum_{i=1}^n B_i \tau_i^2 / \sum_{i=1}^n B_i \tau_i$
f) Unreliable lifetime considering the IRF FWHM (175 ps)

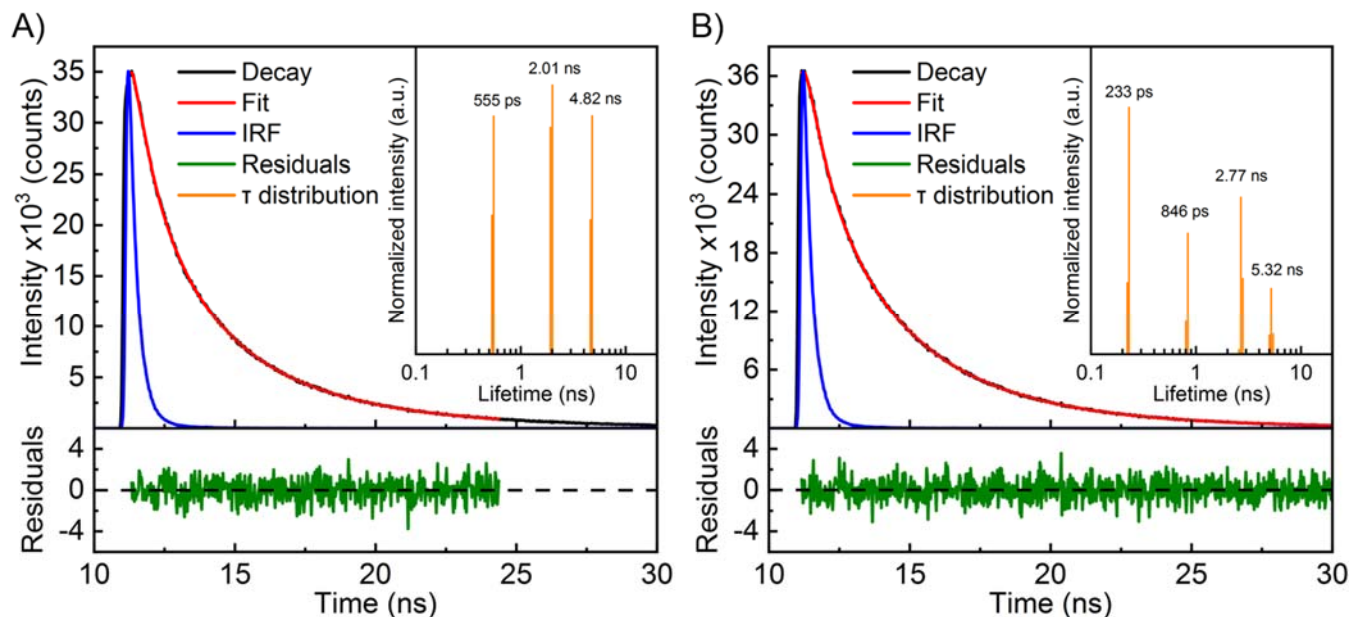


Figure S38. TCSPC decay traces, fits, lifetime distributions - MFGDs in DMF ($\lambda_{ex} = 397$ nm). (A) $\lambda_{em} = 485$ nm, (B) 547 nm.

The large instrument response time at $\lambda_{excitation} = 397$ nm (IRF FWHM of 371 ps), compared to $\lambda_{excitation} = 477$ nm (IRF FWHM of 175 ps), makes the determination of lifetimes inferior to 1.5-1.8 ns unreliable resulting in a high chi-square value for the overall fitting. To confirm our fitting from distribution analysis (Table S4) we also performed a fitting through exponential component analysis (Table S5).

Table S4. PL lifetime fit (distribution analysis) - MFGDs in DMF ($\lambda_{\text{ex}} = 397$ nm, $\lambda_{\text{em}} = 485/547$ nm).

$\lambda_{\text{emission}}$ (nm)	B ^a	f (%) ^b	τ ^c	T ^d	$\langle \tau \rangle$ ^e	χ^2
485	2.8×10^{-2}	0.4	25 ± 1 ps ^f	25 ps	3.35 ns	1.637
	1.6×10^{-1}	6.3	61 ± 1 ps ^f	62 ps		
	1.8×10^{-2}	6.5	555 ± 13 ps ^f	563 ps		
	2.4×10^{-2}	30.9	2.01 ± 0.05 ns	2.04 ns		
	1.8×10^{-2}	55.9	4.82 ± 0.11 ns	4.90 ns		
547	4.1×10^{-2}	5.2	233 ± 5 ps ^f	235 ps	3.48 ns	1.236
	2.0×10^{-2}	9.1	846 ± 17 ps ^f	854 ps		
	3.1×10^{-2}	46.2	2.77 ± 0.07 ns	2.74 ns		
	1.4×10^{-2}	39.4	5.32 ± 0.15 ns	5.32 ns		

- a) Pre-exponential factor
b) Fluorescence intensity percentage
c) Center of gravity of the distribution spike
d) Maximum of the distribution spike
e) Average lifetime $\langle \tau \rangle = \sum_{i=1}^n B_i \tau_i^2 / \sum_{i=1}^n B_i \tau_i$
f) Unreliable lifetime considering the IRF FWHM (371 ps)

Table S5. PL lifetime fit (exponential component analysis) - MFGDs in DMF ($\lambda_{\text{ex}} = 397$ nm, $\lambda_{\text{em}} = 485/547$ nm).

$\lambda_{\text{emission}}$ (nm)	B ^a	f (%) ^b	τ	$\langle \tau \rangle$ ^c	χ^2
485	$(2.7 \pm 1.3) \times 10^{-1}$	9.8 ± 973.4 %	61 ± 5976 ps ^d	3.18 ns	1.044
	$(1.9 \pm 0.2) \times 10^{-2}$	6.3 ± 4.4 %	551 ± 326 ps ^d		
	$(2.4 \pm 0.4) \times 10^{-2}$	28.4 ± 6.8 %	1.94 ± 0.11 ns		
	$(1.9 \pm 0.7) \times 10^{-2}$	55.5 ± 20.0 %	4.71 ± 0.04 ns		
547	$(4.6 \pm 1.2) \times 10^{-2}$	5.7 ± 31.3 %	234 ± 1228 ps ^d	3.44 ns	1.007
	$(2.0 \pm 0.2) \times 10^{-2}$	9.0 ± 3.1 %	834 ± 186 ps ^d		
	$(3.1 \pm 0.2) \times 10^{-2}$	45.3 ± 2.4 %	2.74 ± 0.02 ns		
	$(1.4 \pm 0.3) \times 10^{-2}$	39.9 ± 7.4 %	5.29 ± 0.01 ns		

- a) Pre-exponential factor
b) Fluorescence intensity percentage
c) Average lifetime $\langle \tau \rangle = \sum_{i=1}^n B_i \tau_i^2 / \sum_{i=1}^n B_i \tau_i$
d) Unreliable lifetime considering the IRF FWHM (371 ps)

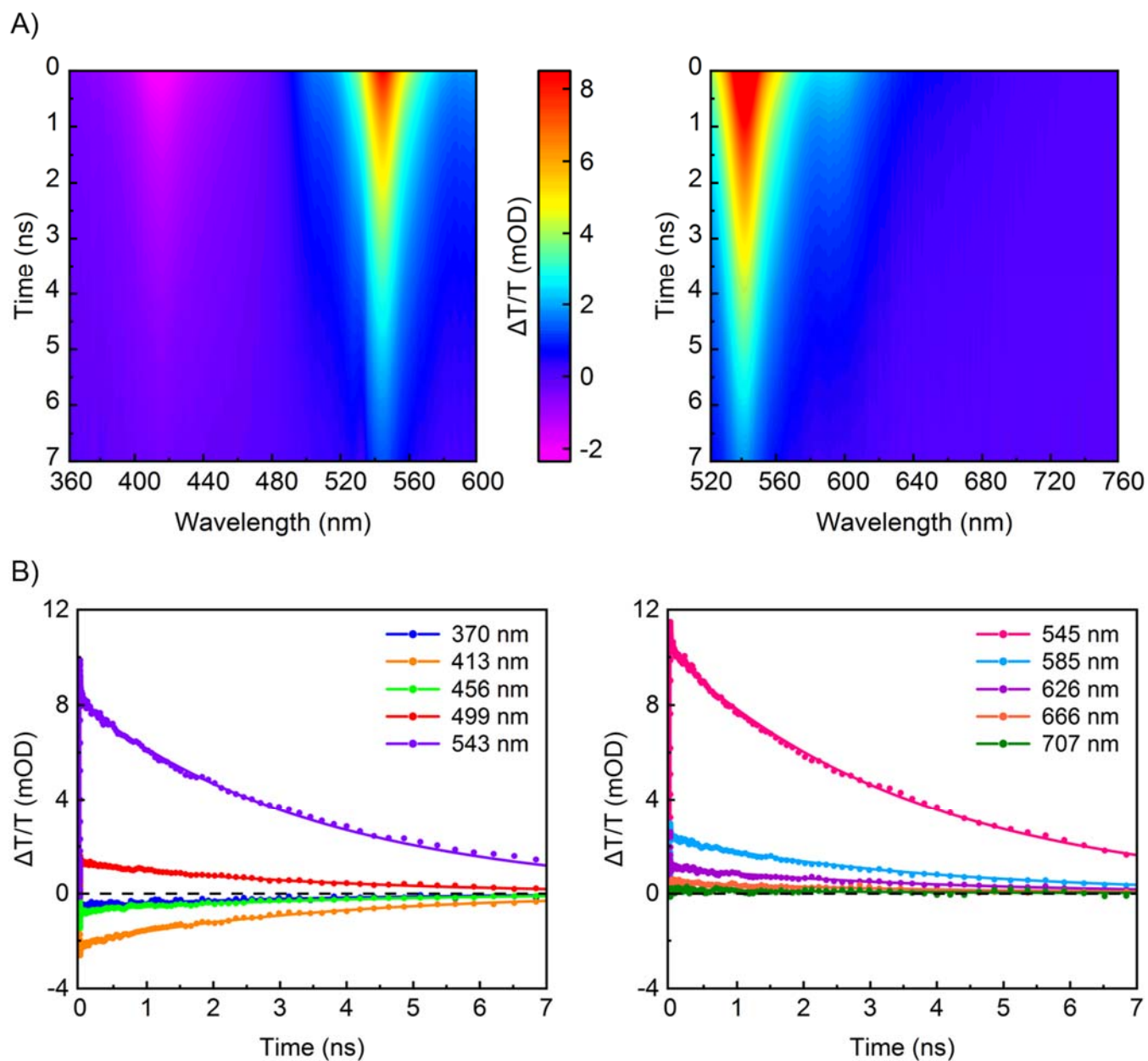


Figure S39. (A) fs-TAS maps (in transmittance) of MFGDs in DMF ($\lambda_{\text{pump}} = 530$ nm, $P = 0.12$ mJ.cm⁻²): in the range 360-600 nm (left), in the range 520-760 nm (right). (B) TAS kinetic traces at given $\lambda_{\text{absorption}}$: in the low-wavelength range (left), in the high-wavelength range (right).

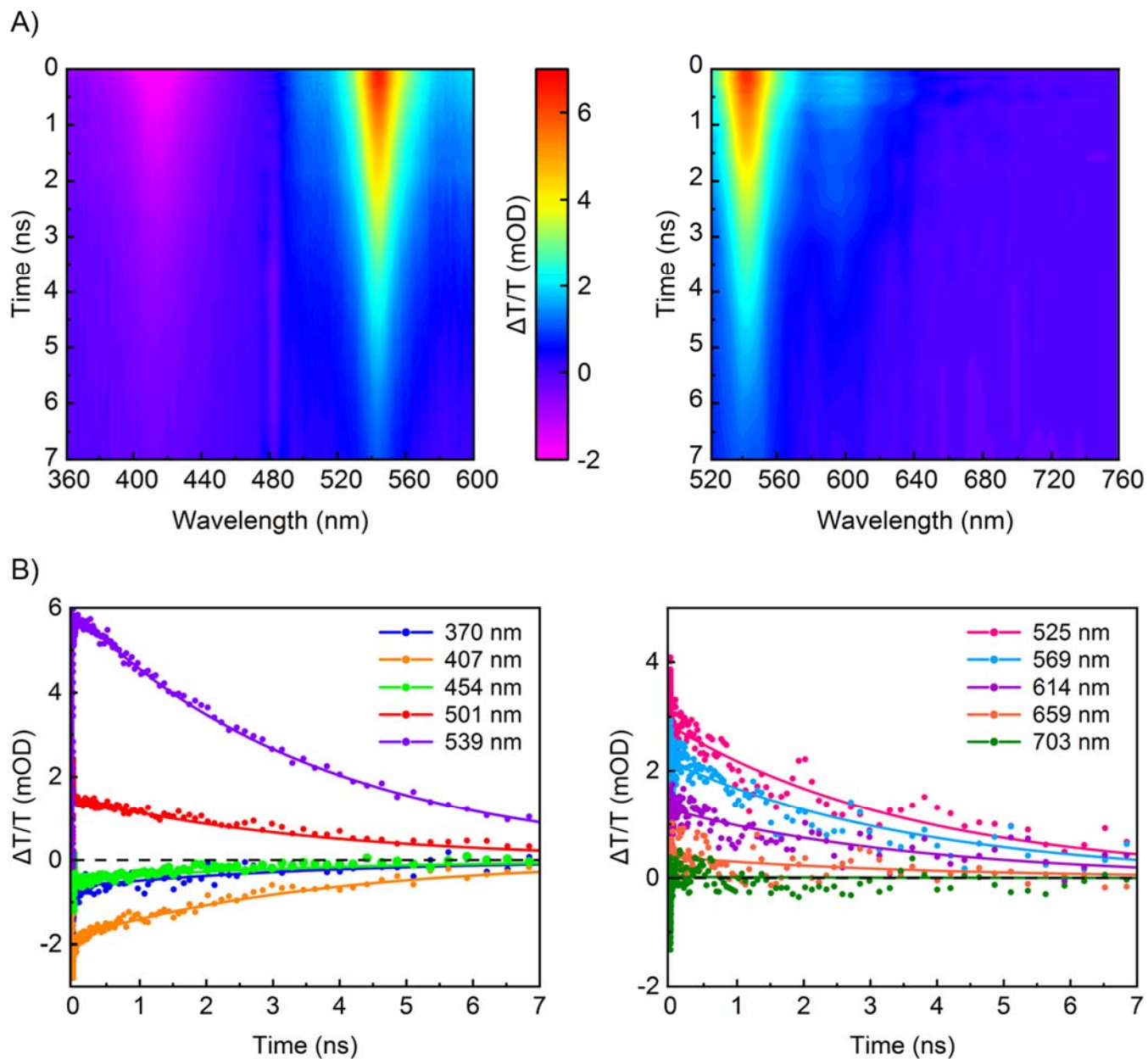


Figure S40. (A) fs-TAS maps (in transmittance) of MFGDs in DMF ($\lambda_{\text{pump}} = 480$ nm, $P = 0.36$ mJ.cm⁻²): in the range 360-600 nm (left), in the range 520-760 nm (right). (B) TAS kinetic traces at given $\lambda_{\text{absorption}}$: in the low-wavelength range (left), in the high-wavelength range (right).

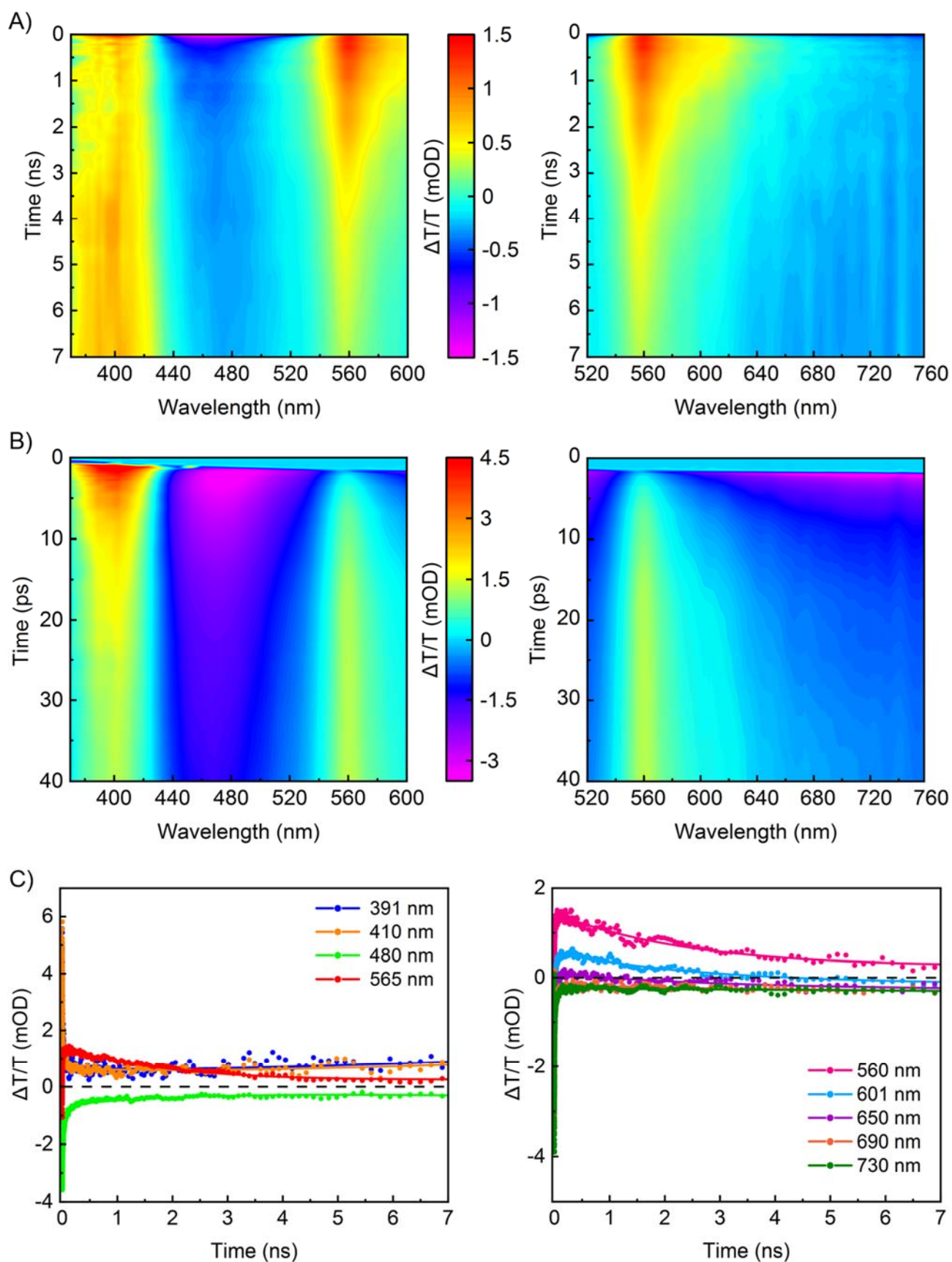


Figure S41. fs-TAS maps (in transmittance) of MFGDs in DMF ($\lambda_{\text{pump}} = 397$ nm, $P = 0.16$ mJ.cm⁻²) (A) at the ns-timescale, (B) at the ps-timescale, in the range 360-600 nm (left), in the range 520-760 nm (right). (C) TAS kinetic traces at given $\lambda_{\text{absorption}}$: in the low-wavelength range (left), in the high-wavelength range (right).

Table S6. fs-TAS deconvolution results of MFGDs in DMF ($\lambda_{\text{pump}} = 530 \text{ nm}$, 480 nm and 397 nm).

$\lambda_{\text{pump}} \text{ (nm)}$	UV window			Vis Window		
	τ	IRF ^a (fs)	RMSE ^b	τ	IRF ^a (fs)	RMSE ^b
530	$1.71 \pm 0.02 \text{ ps}$			$1.54 \pm 0.01 \text{ ps}$		
	$56.6 \pm 1.0 \text{ ps}$	96.9	9.9×10^{-5}	$98.0 \pm 2.0 \text{ ps}$	95.8	1.2×10^{-4}
	$3.64 \pm 0.01 \text{ ns}$			$3.82 \pm 0.01 \text{ ns}$		
480	$1.61 \pm 0.01 \text{ ps}$			$1.28 \pm 0.03 \text{ ps}$		
	$35.9 \pm 0.3 \text{ ps}$	160	1.2×10^{-4}	$14.4 \pm 0.3 \text{ ps}$	130	2.3×10^{-4}
	$3.72 \pm 0.01 \text{ ns}$			$3.76 \pm 0.01 \text{ ns}$		
397	$3.98 \pm 0.03 \text{ ps}$			$4.60 \pm 0.02 \text{ ps}$		
	$43.1 \pm 0.3 \text{ ps}$	48.9	1.9×10^{-4}	$36.0 \pm 0.2 \text{ ps}$	71.9	6.5×10^{-5}
	$2.01 \pm 0.03 \text{ ns}$			$2.55 \pm 0.01 \text{ ns}$		
	$> 8 \text{ ns}$			$> 8 \text{ ns}$		

a) Instrument response function

b) Root mean squared error

For MFGDs, we observe 3 processes from both TCSPC and fs-TAS analyses:

- a major one, at $\sim 4 \text{ ns}$ which is clearly the fluorescence decay of the fluorophore (assumed to be $S_1 \rightarrow S_0$) (see TCSPC results)
- a minor one, of low magnitude, with a few picosecond characteristic delay. The DAS (Figure S43) indicates that this contribution which relaxes with a decay of 4.5 ps corresponds to a broad feature-less excited state absorption of very low intensity when excited at 397 nm . Similar excited-state absorption have already been reported in literature from GDs⁴. By contrast, when excited at 530 nm , an emission occurs with a characteristic decay of 1.7 ps . Literature on GDs has attributed phenomena of comparable lifetimes to an internal conversion process⁵ (i.e. $S_2 \rightarrow S_1$ emission).
- a second minor component occurs on timescales of $\sim 50 \text{ ps}$. The DAS indicate the absence of any characteristic feature for this component at all wavelengths. Such component could be thus attributed to non-radiative decay originating from vibronic thermalization, as such solvent thermalization phenomena are typically in the 10 ps timescale^{6,7}. The very low magnitude of this component reinforces our hypothesis that MFGDs are unable to exchange energy with their environment.

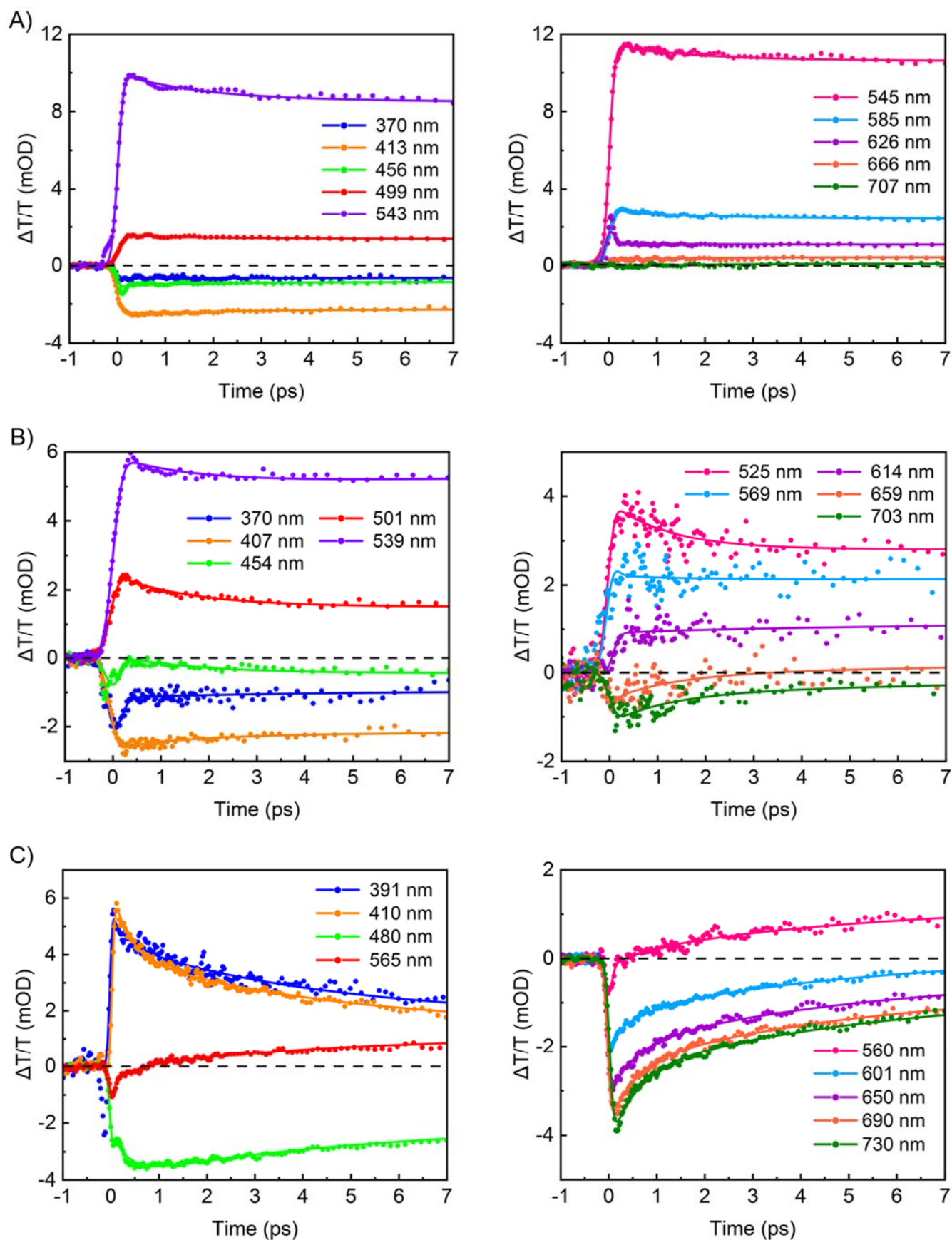


Figure S42. TAS kinetic traces of MFGDs in DMF on a 7-ps window at given $\lambda_{\text{absorption}}$: (A) $\lambda_{\text{pump}} = 530 \text{ nm}$ (0.12 mJ.cm^{-2}), (B) $\lambda_{\text{pump}} = 480 \text{ nm}$ (0.36 mJ.cm^{-2}), (C) $\lambda_{\text{pump}} = 397 \text{ nm}$ (0.16 mJ.cm^{-2}) (C). Left graphs cover the low-wavelength range, right graphs cover the high-wavelength range.

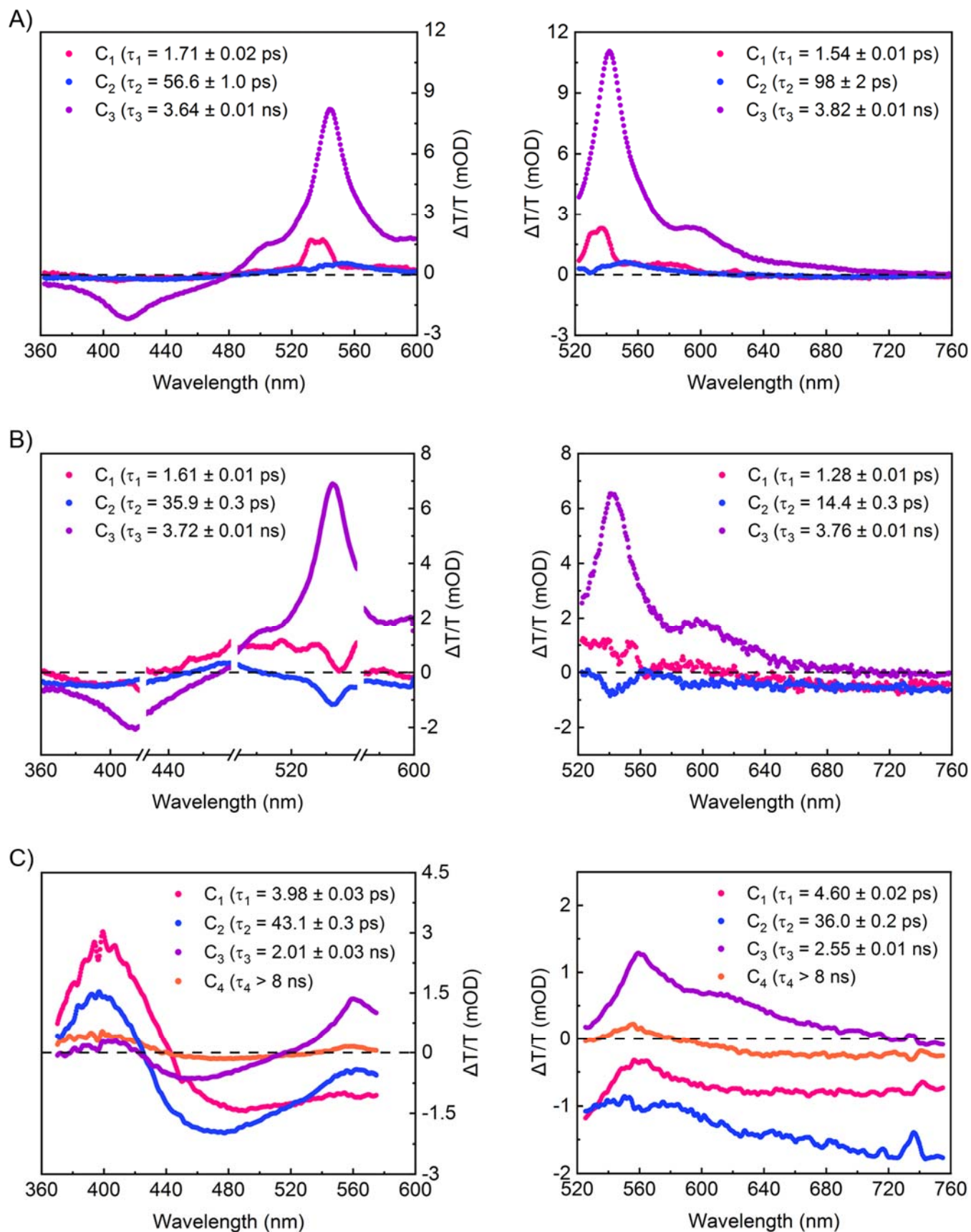


Figure S43. Decay associated spectra (DAS) from fs-TAS measurements of MFGDs in DMF: (A) $\lambda_{\text{pump}} = 530$ nm (0.12 mJ.cm^{-2}), (B) $\lambda_{\text{pump}} = 480$ nm (0.36 mJ.cm^{-2}), (C) $\lambda_{\text{pump}} = 397$ nm, (0.16 mJ.cm^{-2}). Left graphs cover the range 360-600 nm, right graphs cover the range 520-760 nm.

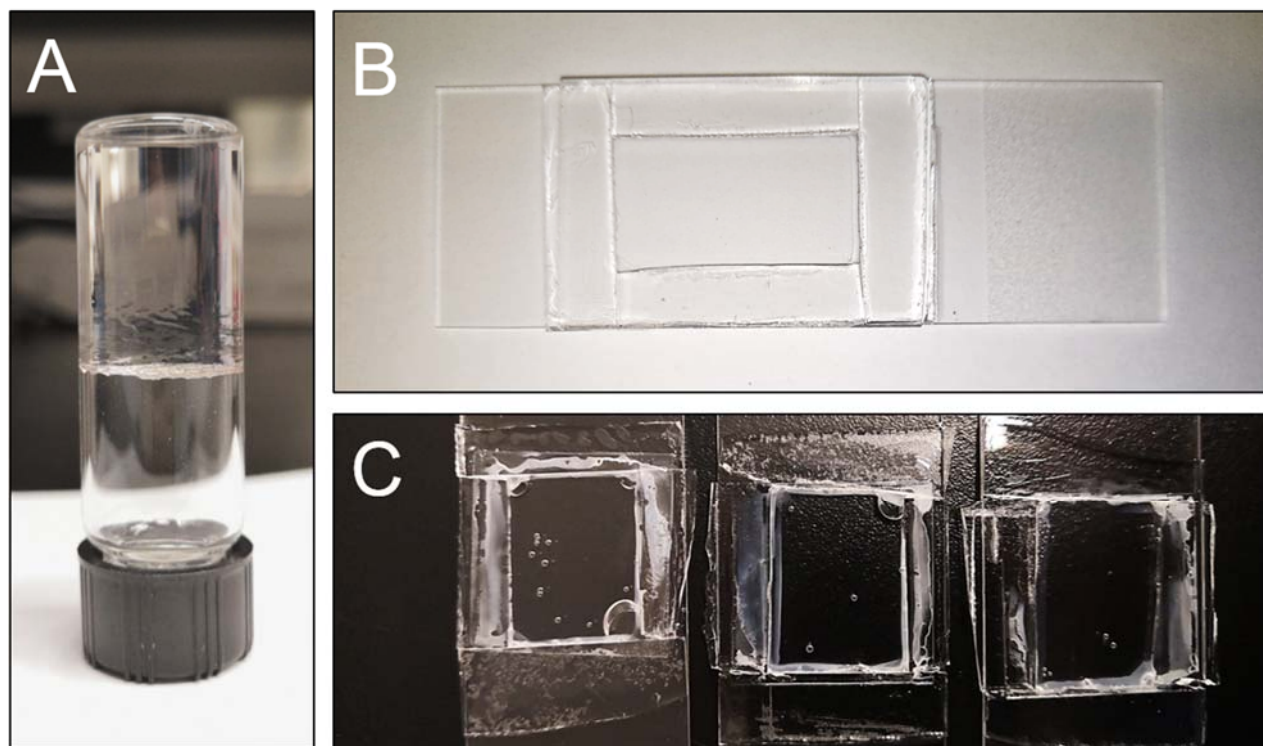


Figure S44. Photograph of a vial containing an aqueous acrylamide-gel dispersing MFGDs (positioned upside-down to show the gelation) (A). Mounted glass-walled pool on a microscope slide designed for MFGDs microscopy studies: before curing (B), after curing (C).

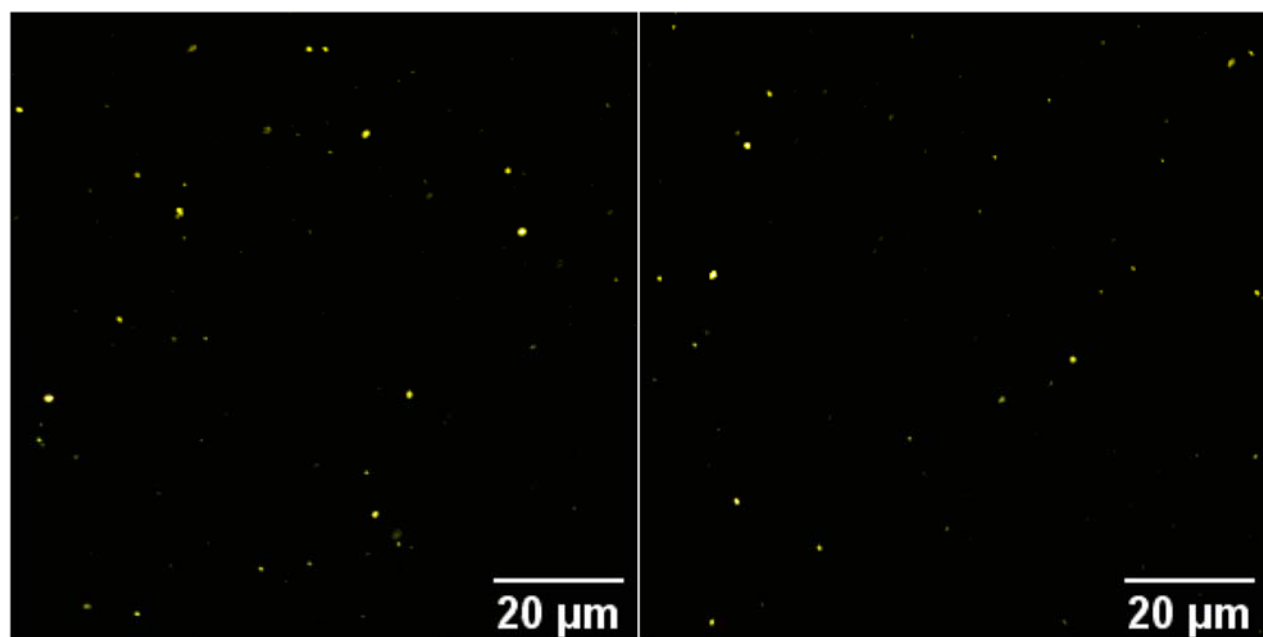


Figure S45. Wide-field fluorescence micrographs of MFGDs dispersed in an aqueous acrylamide gel.

The size of MFGDs is much smaller than the diffraction-limited spatial resolution of the fluorescence imaging experiment, it is thus not possible to distinguish between isolated MFGDs and small aggregates from this experiment. However, TEM images (Figure S15) clearly indicate that MFGDs are well separated. Here, MFGDs are dispersed in a gel containing 80 w% water. In such a medium, MFGDs are expected to be solvated and well separated from each other (Figure S44 for the picture of a MFGDs-containing gel).

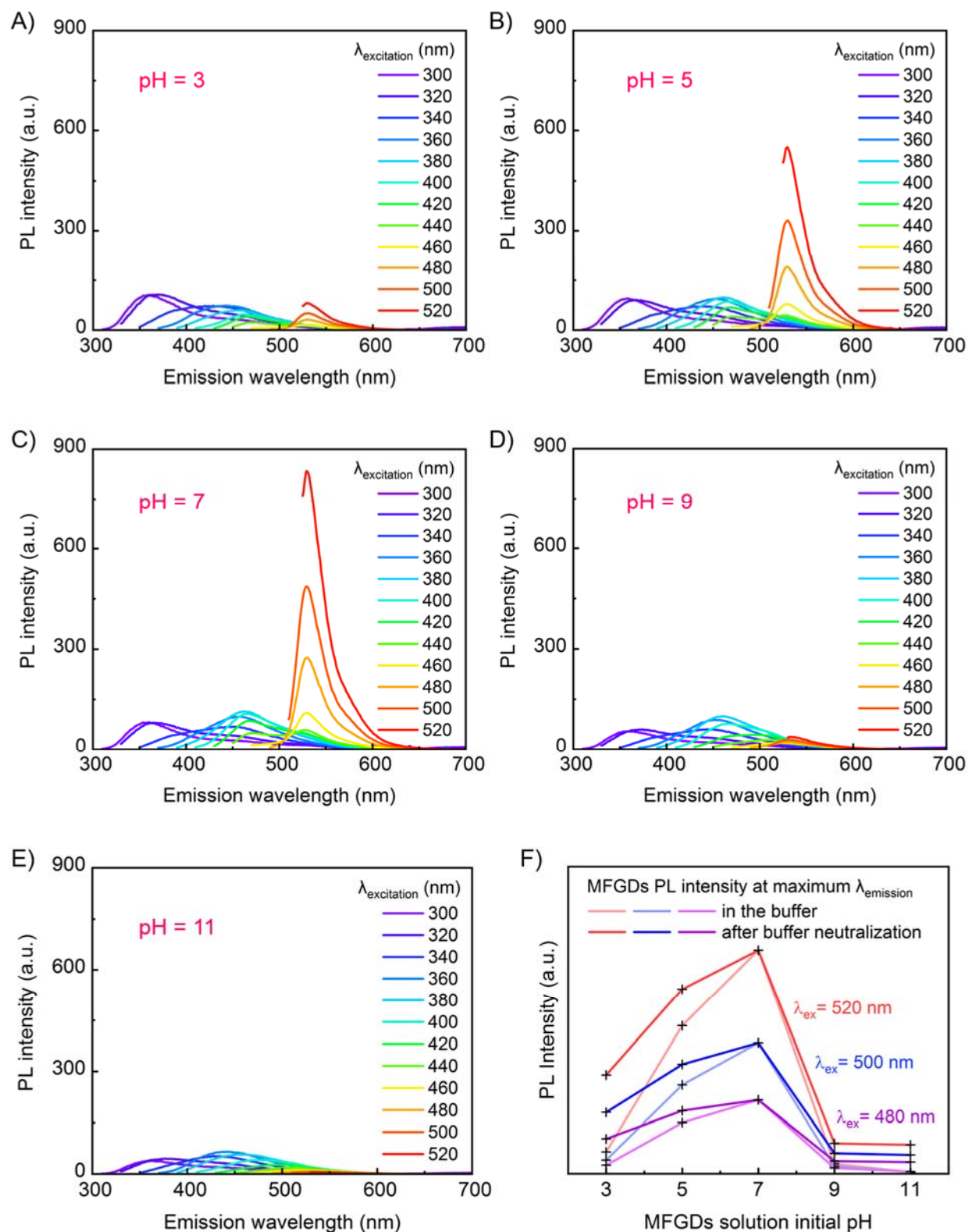


Figure S46. PL spectra of MFGDs in aqueous buffers of different pH at various excitation wavelengths: pH = 3 (A), pH = 5 (B), pH = 7 (C), pH = 9 (D), pH = 11 (E). PL intensity at maximum emission before and after neutralization of the buffers, as a function of their initial pH (F).

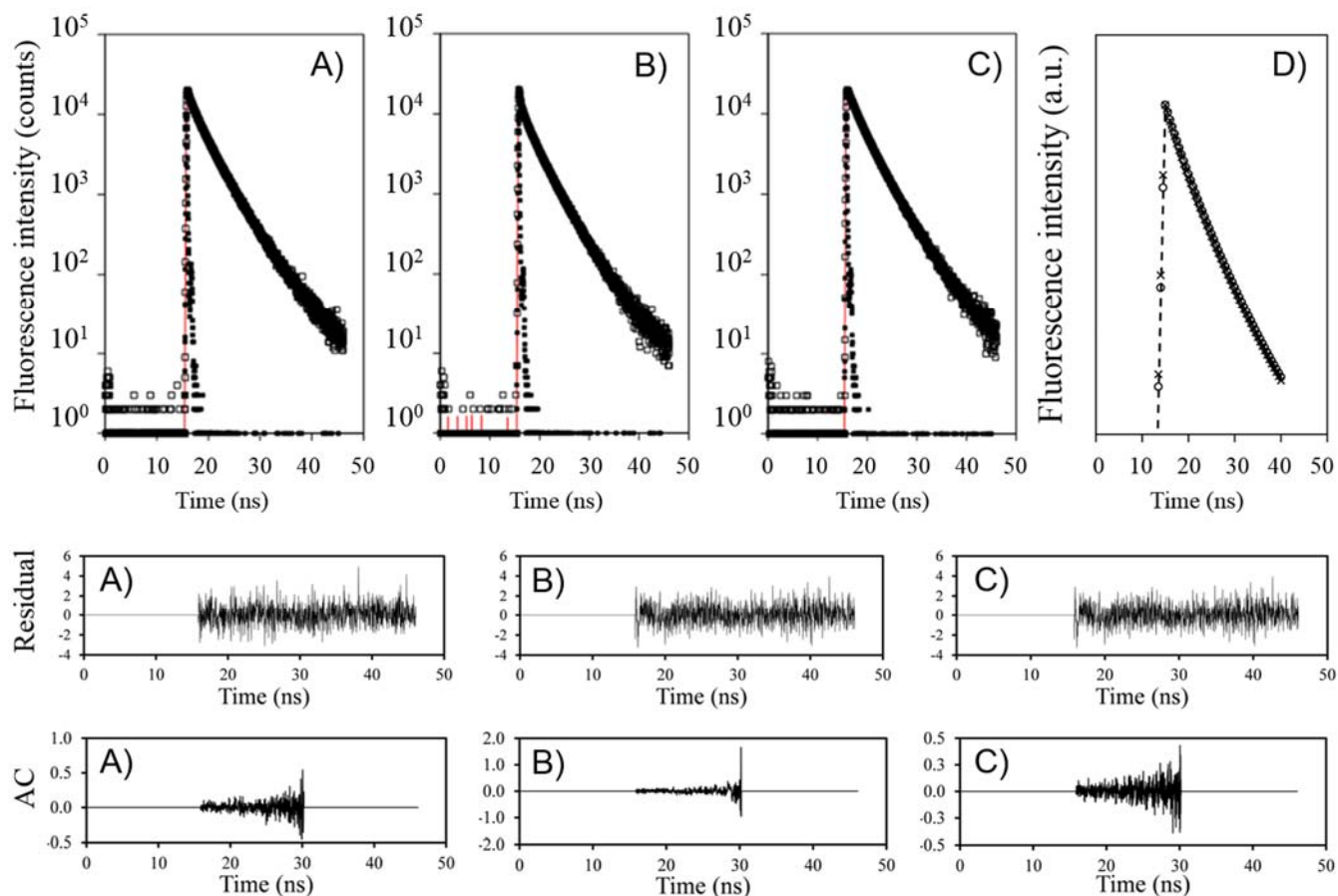


Figure S47. Polarization fluorescence decays with residuals and autocorrelation of the residuals acquired with vertically polarized light at 479 nm and with the emission at 510 nm with the emission polarizer placed A) at the magic angle ($I_{VM}(t)$), B) vertically ($I_{VV}(t)$), and C) horizontally ($I_{VH}(t)$). D) Overlay of the fit of the three decays without the short $\tau_1 \sim 0.4$ ns component: (— — —) $I_{VV}(t)$, (\bullet) $I_{VM}(t)$, and (\times) $I_{VH}(t)$

Figures S47A, B, and C show the fluorescence decays of the dispersions, that were acquired with a vertically polarized excitation and an emission, that was collected with a polarizer oriented at the magic angle ($I_{VM}(t)$), vertically ($I_{VV}(t)$), and horizontally ($I_{VH}(t)$), respectively. The fluorescence decays were fit with a sum of four exponentials and the pre-exponential factors and decay times are listed in Table 1. The only difference between the decays was a short component with a decay time of ~ 0.4 ns whose contribution was most pronounced in the $I_{VV}(t)$ decay and least pronounced in the $I_{VH}(t)$ decay. This short contribution was most likely due to residual light scattered by the nanoparticles. In fact, calculating the average lifetime ($\langle \tau \rangle$) without the short 0.4 ns contribution resulted in the same $\langle \tau \rangle$ value in Table S7. Furthermore, overlapping the fits of the decays without the short τ_1 decay time resulted in the exact same decays in Figure S47D.

Table S7. Pre-exponential factors and decay times retrieved from the fit of the fluorescence decays with a sum of four exponentials. The number average lifetime ($\langle \tau \rangle$) was calculated without the short contribution of $\tau_1 \sim 400$ ps.

	B^a	τ	$f(\%)^b$	$\langle \tau \rangle^c$	χ^2
$I_{VV}(t)$	3.7×10^{-1}	370 ps	6.2	3.21 ns	1.11
	3.6×10^{-1}	2.32 ns	38.4		
	2.7×10^{-1}	4.30 ns	54.2		
	1.0×10^{-3}	24.50 ns	< 0.1		
$I_{VH}(t)$	9.0×10^{-2}	390 ps	1.2	3.09 ns	1.32
	2.3×10^{-1}	1.51 ns	12.4		
	6.0×10^{-1}	3.31 ns	70.1		
	7.6×10^{-2}	6.10 ns	0.2		
$I_{VM}(t)$	2.5×10^{-1}	410 ps	4.0	3.22 ns	1.09
	4.3×10^{-1}	2.35 ns	39.8		
	3.2×10^{-1}	4.30 ns	54.9		
	1.9×10^{-3}	17.1 ns	< 0.1		

a) Pre-exponential factor

b) Fluorescence intensity percentage

c) Average lifetime $\langle \tau \rangle = \sum_{i=1}^n B_i \tau_i^2 / \sum_{i=1}^n B_i \tau_i$

The identical $I_{VV}(t)$, $I_{VH}(t)$, and $I_{VM}(t)$ fluorescence decays suggested that the rotational time of the particles was either much shorter or much longer than $\langle \tau \rangle$. Since the anisotropy (r) is given by Equation S1, where r_0 is the anisotropy at time $t = 0$, a much shorter or much longer ϕ value would imply that r would equal 0 or r_0 , respectively.

$$r = \frac{r_0}{1 + \frac{\langle \tau \rangle}{\phi}} \quad (7)$$

The steady-state fluorescence spectra of the dispersion were acquired with an excitation and emission polarizers that were placed in the vertical and vertical (I_{VV}), vertical horizontal (I_{VH}), horizontal and horizontal (I_{HH}), and horizontal and vertical (I_{HV}) positions. After determining the G-factor at each wavelength ($G = I_{HV}/I_{HH}$), the anisotropy was calculated at each wavelength by applying Equation S2.

$$r = \frac{I_{VV} - G \times I_{VH}}{I_{VV} + 2G \times I_{VH}} \quad (8)$$

The I_{VV} , I_{VH} , I_{HH} , and I_{HV} fluorescence spectra and the anisotropy are presented in Figure S48A. The anisotropy shown in Figure S48B equals 0.042 ± 0.009 and is greater than zero from 500 to 700 nm, with an increasing value at wavelengths greater than 700 nm due to increasing scattering over fluorescence intensity ratio.

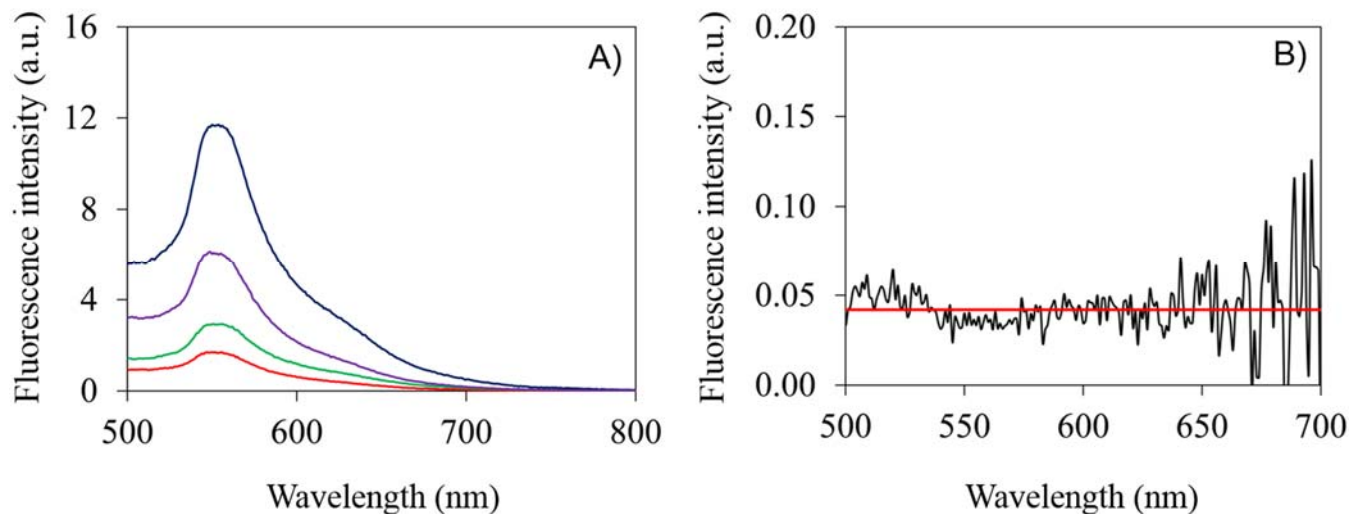


Figure S48. A) Polarization fluorescence spectra for (—) I_{VV} , (—) I_{VH} , (—) I_{HH} , and (—) I_{HV} . B) (—) Fluorescence anisotropy. Horizontal red line represents the average anisotropy.

The non-zero anisotropy in Figure S48B combined with the identical fluorescence decays shown in Figure S47 would thus suggest that characteristic rotational time (ϕ) must be much larger than $\langle \tau \rangle$. This is reasonable considering that an estimation of ϕ of 22 ns can be given according to the following equation:

$$\phi = \frac{4\pi R^3 \eta}{3k_b T} \quad (8)$$

Where R is the hydrodynamic radius of the MFGDs (including its polymeric surrounding layer) and estimated to be around at least 3 nm), η the viscosity of the medium (0.79 mPa.s for DMF at 25 °C), k_b the Boltzmann constant and T the absolute temperature (298 K).

The characteristic rotation time ϕ (22 ns), 8 times larger than $\langle \tau \rangle$, would be too long to be detected in the polarization fluorescence decays. Consequently, the non-zero anisotropy in Figure S48B (indicating that the orientation of the dipole moment of the dyes is preserved in the nanoparticles) combined with the identical fluorescence decays observed in Figures S47 (indicating that the nanoparticles tumble on a time scale that is much longer than the time scale of their fluorescence) suggest that isolated molecular fluorophores are occupying the nanoparticles.

References

- (1) Ferguson, C. J., Hughes, R. J., Nguyen, D., Pham, B. T. T., Gilbert, R. G., Serelis, A. K., Such, C. H., Hawket, B. S. Ab Initio Emulsion Polymerization by RAFT-Controlled Self-Assembly. *Macromolecules* **38**, 2191-2204 (2005).
- (2) Eberhardt, M., Mruk, R., Zentel, R., Théato, P. Synthesis of pentafluorophenyl(meth)acrylate polymers: New precursor polymers for the synthesis of multifunctional materials. *Eur. Polym. J.* **41**, 1569-1575 (2005).
- (3) Kovác, A., Nyerges, B., Izvekov, V. Vibrational Analysis of N-Acetyl- α -D-glucosamine and β -D-Glucuronic Acid. *J. Phys. Chem. B* **112**, 5728-5735 (2008)
- (4) Sciortino, A., Gazzetto, M., Soriano, M. L., Cannas, M., Cárdenas, S., Cannizzo, A., Messina, F. Ultrafast Spectroscopic Investigation on Fluorescent Carbon Nanodots: The Role of Passivation. *Phys. Chem. Chem. Phys.* **21**, 30 (2019)
- (5) Kwon, W., Do, S., Kim, J.-H., Jeong, M. S., Rhee, S.-W. Control of Photoluminescence of Carbon Nanodots via Surface Functionalization Using Para-Substituted Anilines. *Sci. Rep.* **5**, 12604 (2015)
- (6) Balevičius, V., Wei, T., Di Tommaso, D., Abramavicius, D., Hauer, J., Polívka, T., Duffy, C. D. P. The Full Dynamics of Energy Relaxation in Large Organic Molecules: From Photo-Excitation to Solvent Heating. *Chem. Sci.* **10**, 4792-4804 (2019)
- (7) Middleton, C. T., Cohen, B., Kohler, B. Solvent and Solvent Isotope Effects on the Vibrational Cooling Dynamics of a DNA Base Derivative. *J. Phys. Chem. A* **111**, 10460-10467 (2007)